

Uncertainty quantification for predictions of atomistic neural networks

Luis Itza Vazquez-Salazar,^{1, a)} Eric D. Boittier,¹ and Markus Meuwly^{1, b)}

Department of Chemistry, University of Basel, Basel, Switzerland

(Dated: 15 July 2022)

The value of uncertainty quantification on predictions for trained neural networks (NNs) on quantum chemical reference data is quantitatively explored. For this, the architecture of the PhysNet NN was suitably modified and the resulting model was evaluated with different metrics to quantify its calibration, the quality of its predictions, and whether prediction error and the predicted uncertainty can be correlated. The results by training on the QM9 database and evaluating data in the test set within and outside the distribution indicate that error and uncertainty are not linearly related. However, the observed variance can provide insight into the quality of the data used for training. Additionally, the influence of the chemical space covered by the training data set was studied by using a biased database. The results clarify that noise and redundancy complicate property prediction for molecules even in cases for which changes - such as double bond migration in two otherwise identical molecules - are small. The model was also applied to a real database of tautomerization reactions. Analysis of the distance between members in feature space in combination with other parameters shows that redundant information in the training dataset can lead to large variances and small errors whereas the presence of similar but unspecific information returns large errors but small variances. This was, e.g., observed for nitro-containing aliphatic chains for which predictions were difficult although the training set contained several examples for nitro groups bound to aromatic molecules. The finding underlines the importance of the composition of the training data and provides chemical insight into how this affects the prediction capabilities of a ML model. Finally, the presented method can be used for information-based improvement of chemical databases for target applications through active learning optimization.

Keywords: Suggested keywords: Uncertainty Quantification, Machine learning, chemical space, tautomerization, evidential deep learning

^{a)}Electronic mail: luisitza.vazquezsalazar@unibas.ch

^{b)}Department of Chemistry, Brown University, USA; Electronic mail: m.meuwly@unibas.ch

I. INTRODUCTION

Undoubtedly machine learning (ML) models are becoming part of the standard computational/theoretical chemistry tools. This is because it is possible to develop highly accurate trained models in an efficient manner. In chemistry, such ML models are used in various branches ranging from the study of reactive processes,^{1,2} sampling equilibrium states,³ the generation of accurate force fields,⁴⁻⁸ to the generation and exploration of chemical space.^{9,10} Nowadays, an extensive range of robust and complex models can be found¹¹⁻¹⁵. The quality of these models is only limited by the quality and quantity of the data used for training.^{7,16} For the most part, however, the focus was on obtaining more extensive and complex databases as an extrapolation from applications in computer science. Therefore, it is believed that more significant amounts of data will beat the best algorithm¹⁷.

On the other hand it has been found that even the best model can be tricked by poor data quality¹⁸⁻²¹. For example, in malware detection it was found that ML-based models can fail if the training data does not contain the event the model had been designed for.^{18,20} Also, data completeness and quality directly impacts on the forecasting capabilities of such statistical models. The notion of underperforming models trained on low-quality data ("garbage in-garbage out") can be traced back to Charles Babbage.²² The ML community is starting to notice the importance of data quality used for training and the relevance to balance amount of data ("big data") versus quality of data. Using biased and low-quality data in ML can result in catastrophic outcomes²³ such as discrimination towards minorities,²⁴ reduction in patient survival, and the loss of billions of dollars.²⁵ As a result of these findings, the concept of "smart data" emerged.²⁶⁻²⁸ Smart data describes a set of data which contains valid, well-defined and meaningful information that can be processed.²⁷ However, an important consideration concerns the type of data that is required for predicting a particular target property. Although quantum chemical models are trained, for example, on total energies of a set of molecules, it is not evident how to best select the best training set for most accurately predicting energy differences between related compounds, such as structural isomers. For this, the uncertainty on a prediction is a very valuable additional information because this would allow to specifically improve a given training set for predictions that perform unsatisfactorily.

Considering that data generation for training quantum ML models implies the use of considerable amounts of computational power²⁹⁻³¹ which increases the carbon footprint and makes the use of ML difficult for researchers without sufficient resources it is essential to optimize the full workflow from conception to a trained model. With this in mind, the concept of smart data is of paramount importance for conceiving future ML models in chemistry. This necessity has been considered in previous reviews about ML in chemistry^{7,16}; however, it is still poorly understood how the training data influences the outcomes of ML methods. One such effort quantitatively assessed the impact of different commonly used quantum chemical databases on predicting specific chemical properties.³² The results showed that the predictions made with ML are heavily affected by data redundancy and noise implicit in the generation of the training dataset.

Identifying missing/redundant information in chemical databases is a challenging but necessary step to ensure the best performance for ML models. In transfer learning from a lower level of quantum chemical treatment (Møller-Plesset second order theory - MP2) to the higher coupled cluster with singles, doubles and perturbative triples (CCSD(T)) it has been found for the H-transfer barrier height in malonaldehyde that it is rather the selection of geometries included in TL than the number of additional points.³³ It is also likely that depending on the chemical target quantity of interest the best database differs from the content of a more generic chemical database. Under such circumstances, uncertainty quantification (UQ) on the prediction can provide valuable information on how prediction quality depends on the underlying database used for training the statistical model. UQ of quantum ML usually involves training several models^{34,35}, which implies a high computational cost, to obtain a mean value and a variance. However, as ML models become more prevalent in different high-risk fields, new efficient techniques for UQ have emerged.^{36,37} Among those techniques, it is of particular interest to use those that involve the determination of variance in a single deterministic model because it is computationally cheaper and can be used for active learning. In the present work, we explore the advantage of using a method called 'Deep Evidential Regression'³⁸ that allows us to predict the variance in a prediction using a single deterministic model.

The present article is structured as follows. First, the methods section describes the assumptions and modifications made to the PhysNet model to be used for variance prediction. Additionally, metrics used for optimizing the hyperparameter λ of the new architecture are reported together with the test performed. Next, the results for the calibration procedure and experiments relating the error and variance with the chemical composition of the database are analyzed. Finally, conclusions are drawn, and it is set the stage for future studies.

II. METHODS

As a regression model, PhysNet³⁹ was selected for the present purpose. PhysNet was implemented within the PyTorch framework⁴⁰ to make it compatible with modern GPU architectures and in line with community developments. The original architecture of PhysNet was modified to output the energy and three extra parameters that will be required for the representation of the uncertainty (Figure 1). Following earlier work³⁸, it is assumed that the targets to predict (here energies E_i for samples i) are drawn from an independent and identically distributed (i.i.d) Gaussian distribution with unknown mean (μ) and variance (σ^2) for which probabilistic estimates are desired:

$$(E_1, \dots, E_N) \approx \mathcal{N}(\mu, \sigma^2)$$

For modeling the unknown energy distribution, a prior distribution is placed on the unknown mean (μ) and variance (σ^2). Following the assumption that the values are drawn from a Gaussian distribution, the mean can be represented by a Gaussian distribution and the variance as an Inverse-Gamma distribution

$$\mu \sim \mathcal{N}(\gamma, \sigma^2 \nu^{-1}), \quad \sigma^2 \sim \Gamma^{-1}(\alpha, \beta)$$

where $\Gamma(\cdot)$ is the gamma function, $\gamma \in \mathbb{R}$, $\nu > 0$, $\alpha > 1$ and $\beta > 0$.

The desired posterior distribution has the form:

$$q(\mu, \sigma^2) = p(\mu, \sigma^2 | E_1, \dots, E_N).$$

where p indicates a generic distribution. Following the chosen representations for mean and variance, it is assumed that the posterior distribution can be factorized as $q(\mu, \sigma^2) = q(\mu)q(\sigma^2)$. Consequently, the joint higher-order, evidential distribution is represented as a Normal-Inverse Gamma distribution (Figure 1) with four parameters ($\mathbf{m} = \{\gamma, \nu, \alpha, \beta\}$) that represent a distribution over the mean and the variance.

$$p(\mu, \sigma^2 | \gamma, \nu, \alpha, \beta) = \frac{\beta^\alpha \sqrt{\nu}}{\Gamma(\alpha) \sqrt{2\pi} \sigma^2} \left(\frac{1}{\sigma^2} \right)^{\alpha+1} \text{Exp} \left(-\frac{2\beta + \nu(\gamma - \mu)^2}{2\sigma^2} \right) \quad (1)$$

The four parameters that represent the Normal-Inverse Gamma distribution are obtained as the output of the final layer of the trained PhysNet model (Figure 1) and the final energy for a molecule composed of N atoms is obtained by summation of the atomic energy contributions E_i :

$$E = \sum_{i=1}^N E_i \quad (2)$$

In a similar fashion, the values for the three parameters (ν, α , and β) that describe the distribution of the variance for a molecule composed of N atoms are obtained by summation of the atomic contributions and are then passed to a softplus activation function to fulfill the conditions given for the distribution ($\gamma \in \mathbb{R}$ and $\nu, \alpha, \beta > 0$)

$$\begin{aligned} \alpha &= \log \left(1 + \exp \left(\sum_{i=1}^N \alpha_i \right) \right) + 1 \\ \beta &= \log \left(1 + \exp \left(\sum_{i=1}^N \beta_i \right) \right) \\ \nu &= \log \left(1 + \exp \left(\sum_{i=1}^N \nu_i \right) \right) \end{aligned} \quad (3)$$

Finally, the expected mean (Equation 4), and the aleatory (Equation 5) and epistemic (Equation 6) uncertainty of predictions can be calculated as:

$$\mathbb{E}[\mu] = \gamma \quad (4)$$

$$\mathbb{E}[\sigma^2] = \frac{\beta}{\alpha - 1} \quad (5)$$

$$\text{Var}[\mu] = \frac{\beta}{\nu(\alpha - 1)} \quad (6)$$

Including the new parameters in the output of the neural network changes the loss function of the model. The new loss function consists of a dual-objective loss $\mathcal{L}(x)$ with two terms: the

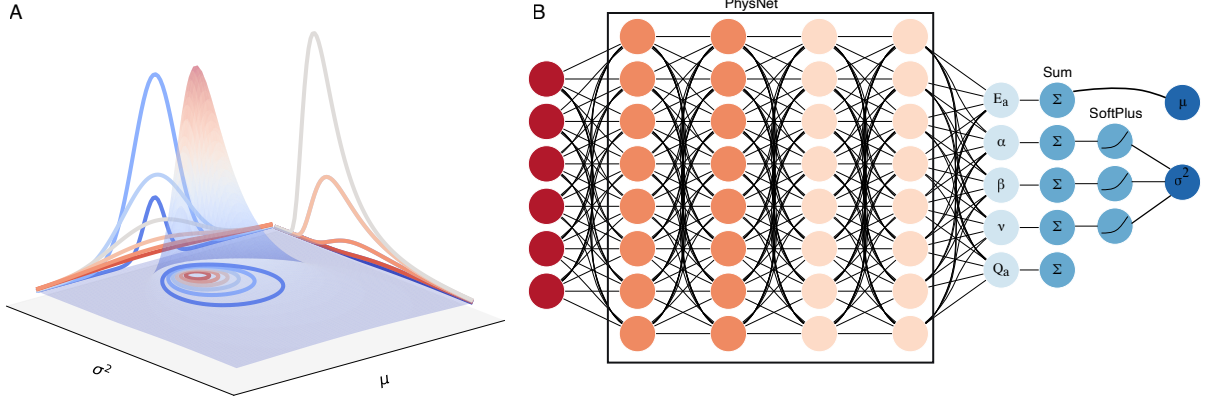


FIG. 1. Modified PhysNet for uncertainty quantification. **A** Schematic 3D representation of the Negative Inverse Gamma distribution as a function of the mean (μ) and the variance (σ^2) (See Equation 1). **B** The modified architecture of PhysNet for the addition of the 'evidential' layer. The input layer receives atomic positions, atomic numbers, charges, and energies. In the next step, those values are passed to the regular architecture of PhysNet. The final layer is modified to output five values (E_a , Q_a , α , β , and ν) per each atom in a molecule. In the next step, the values of the outputs are summed by each molecule. Then, the three extra parameters are passed to a SoftPlus activation function (See Equation 3). The final output of the model are the values for that characterize the Normal Inverse Gamma distribution. The mean value for the prediction (Equation 4) corresponds to the energy of the predicted molecule, and the parameters to determine the variance of the predicted energy which can be obtained using Equations 5 and 6.

first term maximizes model fitting and the second penalizes incorrect predictions according to

$$\mathcal{L}(x) = \mathcal{L}^{\text{NLL}}(x) + \lambda(\mathcal{L}^{\text{R}}(x) - \varepsilon) \quad (7)$$

In equation 7, the first term corresponds to the negative log-likelihood (NLL) of the model evidence that can be represented as a Student- t distribution (Equation 8)

$$\mathcal{L}^{\text{NLL}}(x) = \frac{1}{2} \log\left(\frac{\pi}{\nu}\right) - \alpha \log(\Omega) + \left(\alpha + \frac{1}{2}\right) \log((y - \gamma)^2 \nu + \Omega) + \log\left(\frac{\Gamma(\alpha)}{\Gamma(\alpha + \frac{1}{2})}\right) \quad (8)$$

where $\Omega = 2\beta(1 + \nu)$ and y is the value predicted by the neural network. For details of the derivation of this equation see Ref.³⁸. The second term in Equation 7, $\mathcal{L}^{\text{R}}(x)$, corresponds to a regularizer that minimizes the evidence for incorrect predictions (Equation 9).

$$\mathcal{L}^{\text{R}}(x) = |y - \gamma| \cdot (2\nu + \alpha) \quad (9)$$

The hyperparameter λ controls the influence of uncertainty inflation on the model fit and can be calibrated to obtain more confident predictions. For $\lambda = 0$, the model is overconfident. i.e. results are less likely to be correct. Alternatively, for $\lambda > 0$, the variance is inflated, resulting in underconfident predictions.

The neural network architecture was that of standard PhysNet, with 5 modules consisting of 2 residual atomic modules and 3 residual interaction modules. Finally, the result is pooled into one residual output module. The number of radial basis functions was kept at 64, and the dimensionality of the feature space was 128. Electrostatic and dispersion corrections were not used for the training to keep the model as simple as possible. All other parameters were identical to the standard version of PhysNet³⁹, unless mentioned otherwise.

For training, a batch size of 32 and a learning rate of 0.001 were used. An exponential learning rate scheduler with a decay factor of 0.1 every 1000 steps and the ADAM optimizer⁴¹ with a weight decay of 0.1 were employed. An exponential moving average for all the parameters was used to prevent overfitting. A validation step was performed every five epochs.

A. Hyperparameter Optimization

The hyperparameter λ in equation 7 was optimized by training a range of models with different values of λ , using a portion of the QM9 dataset consisting of 31250, 25000 structures for training, 3125 for validation and the remaining 3125 for testing. Models were trained for 1000 epochs. The values for λ considered were 0.01, 0.1, 0.2, 0.4, 0.5, 0.75, 1.0, 1.5, and 2.0.

B. Metrics for Model Assessment and Classification

In order to compare the performance/quality of the trained models, suitable metrics are required. These metrics are used to select the best value for the hyperparameter λ . Different metrics that have been reported in the literature^{42–44} were evaluated.

The first metric considered is the Root Mean Variance (RMV) defined as:

$$\text{RMV}(j) = \sqrt{\frac{1}{|B_j|} \sum_{t \in B_j} \sigma_t^2} \quad (10)$$

Here, σ_t^2 is the variance in a given bin B_j . For the construction of the bins B_j the data is first ranked with respect to the variance and then split in N bins $\{B_j\}_{j=1}^N$.

The next metric was the empirical Root Mean Squared Error (RMSE):

$$\text{RMSE}(j) = \sqrt{\frac{1}{|B_j|} \sum_{t \in B_j} (y_i - \hat{y}_t)^2} \quad (11)$$

where y_i is the i -th prediction and \hat{y}_t is the average value of the prediction in a bin B_j . Using equations 10 and 11, the Expected Normalized Calibration Error (ENCE):

$$\text{ENCE} = \frac{1}{N} \sum_{j=1}^N \frac{|\text{RMV}(j) - \text{RMSE}(j)|}{\text{RMV}(j)} \quad (12)$$

can be obtained. Additionally, it is possible to quantify the dispersion of the predicted uncertainties for which the Coefficient of Variation (C_v) is

$$C_v = \frac{1}{\mu_\sigma} \sqrt{\frac{1}{N-1} \sum_{i=1}^N (\sigma_i - \mu_\sigma)^2} \quad (13)$$

In equation 13, μ_σ is the mean predicted standard deviation and σ_t is the predicted standard deviation for N samples.

The last metric used for the characterization of the predicted variance of the tested models is the 'sharpness'

$$\text{sha} = \frac{1}{N} \sum_{i=1}^N \text{var}(F_n) \quad (14)$$

In equation 14, the value $\text{var}(F_n)$ corresponds to the variance of the random variable with cumulative distribution function F at point n .⁴³ The purpose of this metric is to measure how close the predicted values of the uncertainty are to a single value.⁴⁵

In addition to the above metrics, calibration diagrams were constructed with the help of the uncertainty toolbox suite.⁴⁶ Calibration diagrams report the frequency of correctly predicted values in each interval relative to the predicted fraction of points in that interval.^{43,47} Another interpretation of the calibration diagram is to quantify the 'honesty' of a model by displaying the true probability in which a random variable is observed below a given quantile; if a model is calibrated this probability should be equal to the expected probability in that quantile.⁴⁶

The results obtained for the test dataset were then classified into four different categories following the procedure described in Kahle and Zipoli.⁴⁸ For the present purpose, ε^* = MSE (mean squared error) and σ^* = MV (mean variance), and the following classes were distinguished:

- True Positive (TP): $\varepsilon_i > \varepsilon^*$ and $\sigma_i > \sigma^*$. The NN identifies a molecule with a large error through a large variance. In this case, it is possible to add training samples with relevant chemical information to improve the prediction of the identified TP. Alternatively, additional samples from perturbed structures for a particular molecule could be added to increase chemical diversity.
- False Positive (FP): $\varepsilon_i < \varepsilon^*$ and $\sigma_i > \sigma^*$ in which case the NN identifies a molecule as a high-error point but the prediction is correct. In this case, the model is underconfident about its prediction.
- True Negative (TN): $\varepsilon_i < \varepsilon^*$ and $\sigma_i < \sigma^*$. Here the model recognizes that a correct prediction is made with a small value for variance. For such molecules the model has sufficient information to predict them adequately by assigning a small variance. Therefore, the model does not require extra chemical information for an adequate prediction.
- False Negative (FN): $\varepsilon_i > \varepsilon^*$ and $\sigma_i < \sigma^*$. The model is confident about its prediction for this molecule but it actually performs poorly on it. One possible explanation for this behaviour is that molecules in this category are rare⁴⁹ in the training set. The model recognizes them with a small variance but because there is not sufficient information the target property (here energy) can not be predicted correctly.

In the above classifications, i refers to a particular molecule considered for the evaluation. The classification relies on the important assumption that the MSE and the MV are comparable in magnitude which implies that the variance predicted by the model is a meaningful approximation to the error in the prediction. A second desired requirement is to assure the validity of the classification procedure and that the obtained variance is meaningful is that $\text{MSE} > \text{MV}$. This requirement is a consequence of the bias-variance decomposition of the squared error⁵⁰

$$\begin{aligned} \mathbb{E}(\text{MSE}) &= \mathbb{E}[(y(x) - \mu(x))^2 | x = x_0] \\ &= \underbrace{\sigma^2}_{\text{Irreducible Error}} + \underbrace{[\mathbb{E}\mu(x_0) - y(x_0)]^2}_{\text{Bias}^2} + \underbrace{\mathbb{E}[\mu(x_0) - \mathbb{E}\mu(x_0)]^2}_{\text{Variance}} \end{aligned} \quad (15)$$

Equation 15 states that the expected value (\mathbb{E}) of the MSE consists of three terms: the irreducible error, the bias, and the variance. Therefore, the MSE will always be smaller than the variance except for the case that $\mu(x) = y$ for which those quantities are equal.⁵¹

As a measure of the overall performance of the model, the *accuracy* is determined as⁵²:

$$\text{ACC} = \frac{N_{\text{TP}} + N_{\text{TN}}}{N_{\text{TP}} + N_{\text{FN}} + N_{\text{TN}} + N_{\text{FP}}} \quad (16)$$

In equation 16, N_{TP} , N_{TN} , N_{FP} , and N_{FN} refers to the number of true positive, true negative, false positive, and false negative samples, respectively. Additionally, it is possible to compute the true positive rate (R_{TP}) or *sensitivity* as:

$$R_{\text{TP}} = \frac{N_{\text{TP}}}{N_{\text{TP}} + N_{\text{FN}}} \quad (17)$$

As a complement to equation 17, the true positive predictive value (P_{TP}) or *precision* is

$$P_{\text{TP}} = \frac{N_{\text{TP}}}{N_{\text{TP}} + N_{\text{FP}}} \quad (18)$$

C. Model Performance for Tautomerization

As a final test, the performance of the evidential model was evaluated using a subset of the Tautobase⁵³, a public database containing 1680 pairs. Previously, those molecules were calculated at the level of theory of the QM9 database.^{32,54} For the purpose of the present work, only molecules that contain less than nine heavy atoms were considered. Three neural

networks with λ values of 0.2, 0.4, and 0.75 were trained with the QM9 database. The QM9 database was filtered to remove molecules containing fluorine and those that did not pass the geometry consistency check. The size of final database size was 110 426 molecules. That number was split on 80 % for training, 10% for validation and 10% for testing. The three models were trained for 500 epochs with the same parameters as for the hyperparameter optimization.

III. RESULTS

In this section the calibration of the network is considered and its performance for different choices of the hyperparameter is assessed. Then, an artificial bias experiment is carried out and finally, the model is applied to the tautomerization data set. Before detailing these results, a typical learning curve for the model is considered in Figure SIS1. As expected, the root mean squared error obtained for the test set decreases with increasing number of samples.

A. Calibration of the Neural Network

The selection of the best value for the hyperparameter λ can be related to the calibration of the neural network model. Ideally, a calibrated regression model should fulfill the condition⁴² that

$$\forall \sigma : \mathbb{E}_{x,y}[(\mu(x) - y)^2 | \sigma(x)^2 = \sigma^2] = \sigma^2$$

where \mathbb{E} is the expected value for the squared difference of the predicted mean evaluated at x minus the observed value y . In other words: the squared error for a prediction can be directly related to the variance predicted by the model.⁴²

Figure 2 compares the root mean squared error with the root mean variance for a given number of bins (100) and shows that the correlation between RMSE and RMV can change between different intervals. Additionally, the slope of the data can be used as an indicator as to whether the model over- or underestimates the error in the prediction. A slope closer to 1 indicates that the model is well-calibrated. Consequently, the predicted variance can

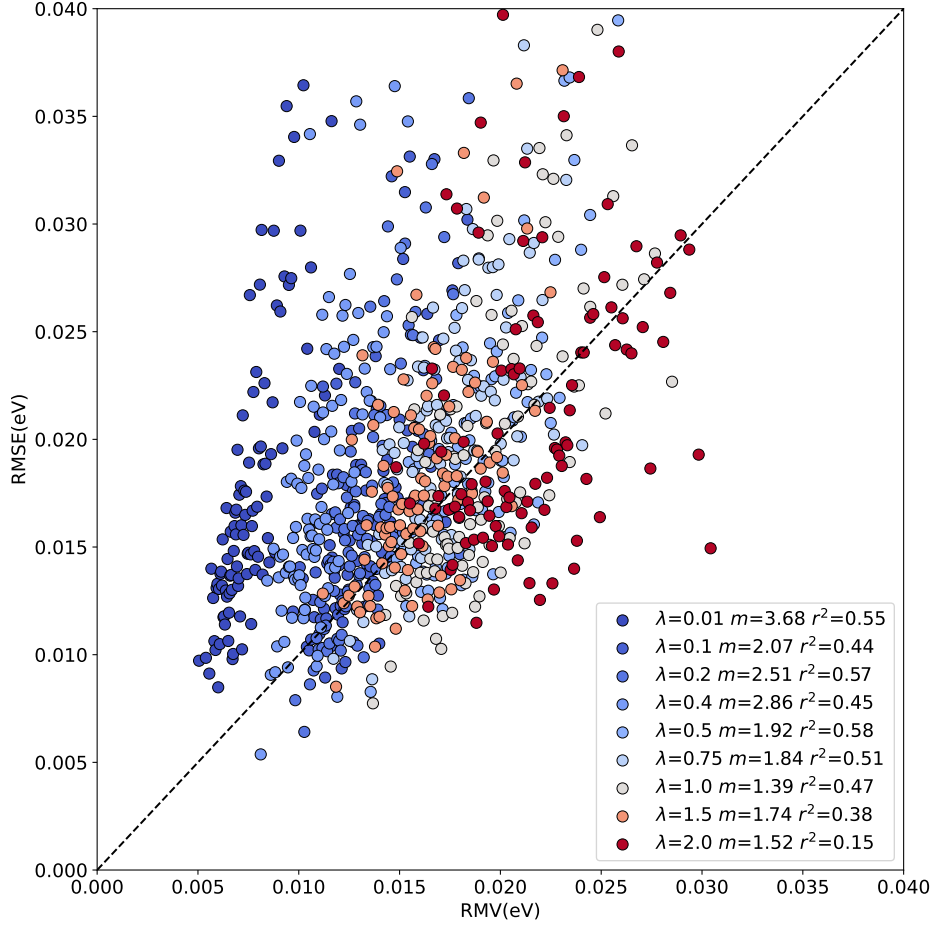


FIG. 2. Empirical root mean squared error compared with the root mean variance of the evidential model trained on 25000 structures from the QM9 database. The values were divided in 100 bins ranked with respect to the predicted variance, 25 bins with 32 samples and 75 with 31 samples were considered. The value of λ together with the slope (m) from a linear regression analysis and the Pearson correlation coefficient (r^2) are given in the legend.

be used as an indicator of the error with respect to the value to be predicted. The results in Figure 2 also show that smaller values of $\lambda = (0.01, 0.2, 0.4)$ result in increased slopes of the RMSE versus RMV curve, i.e. leads to less well-calibrated models, resulting in a model that is overconfident in its predictions. Results that are more consistent with a slope of 1 are obtained for $\lambda = 1$. However, for all trained models it is apparent that RMSE and RMV are not related by a “simple” linear relationship as is sometimes assumed in statistical modeling.

In previous studies,⁴³ the dispersion of the predicted standard deviation was considered as

a measure of the quality of a regression model. Hence a wider distribution of the predicted standard deviation by the model is desired. To remove the influence of pronounced outliers, Figure 3A shows the distributions up to 99% of the predicted variance. It is clear that the center of the distribution, and its width, depend on λ . Larger values of the hyperparameter lead to wider distributions. However, the displacement of the center of mass of the distribution indicates that the standard deviation will be consistently overestimated. Also, $p(\sigma)$ is not Gaussian but rather resembles the inverse gamma distribution that was used as prior for the variance.

Predicted standard deviations from machine learned models must follow some characteristics that help to assess the quality of model predictions.⁴³ Among those characteristics, it is expected that the distribution of the predicted variance is narrow, i.e. will be 'sharp'. This has two objectives, the first is that the model returns uncertainties that are as tight as possible to a specific value.⁴⁵ With this property the model gains confidence on its prediction. The second goal of a 'sharp' model is that it is able to capture the 'trueness'⁵⁵, i.e. the distance between the true value and the mean of the predictions, on the forecast. Another desired characteristic is that $p(\sigma)$ is disperse and does not return a constant value for the uncertainty which would make the model likely to fail for predictions on molecules outside the training data and compromise its generalizability.

The previously described characteristics of the distribution of uncertainties are related to the value of the hyperparameter λ on the loss function (Equation 7) because, as it can be seen in Figure S4, that the MSE by percentile is independent on the choice of λ . Therefore, the model should be calibrated by selecting a value of the hyperparameter that fulfills the desired characteristics for the distribution of uncertainties.

From Figure 3A, it is observed that the spread of the distribution of standard deviations increases with increasing λ . However, the second desired feature for those distribution - sharpness - decreases with increasing λ to become almost constant for $\lambda \geq 0.75$. In consequence of this contradictory behaviour, it is necessary to find a value of λ that yields an accurate estimation of the uncertainty but it does not return a distribution of uncertainties but rather a constant value for each case. It is important to notice that both characteristics,

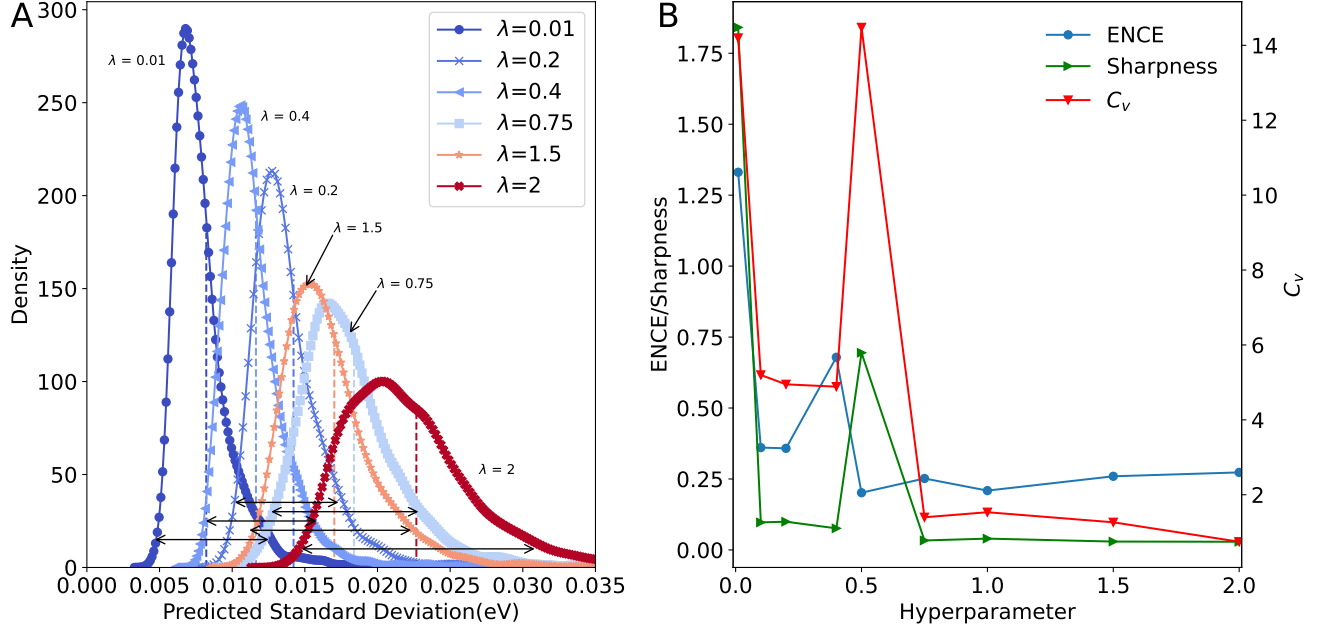


FIG. 3. Metrics for the distribution of predicted variance. **A** Kernel density estimate of standard deviation ($\sigma = \sqrt{\text{Var}}$) for different values of hyperparameter λ . Values up to the 99% percentile of the variance were considered. The internal arrows show the 'width' of the distributions. Dotted lines inside the distribution report their sharpness. Not all distributions are shown for clarity. **B** Evolution of the Expected Normalized Calibration Error (ENCE), sharpness, and the Coefficient of Variation (C_v) depending on λ .

sharpness and width of the distribution, are equally important and one of them should not be sacrificed in favour of the other.⁴³ In other words: a calibrated model is characterized by uncertainty distributions with a certain sharpness and a certain width.

A deeper understanding of the difference between the error of a predicted value and the predicted variance can be obtained through the ENCE (Equation 12) as described in the methods section. This metric is similar to the expected calibration error used in classification. The ENCE quantifies the probability that the model incorrectly predicts the uncertainty of the prediction made. Figure 3B reports the values of ENCE (blue line) and shows that, typically, smaller values for ENCE are expected for increasing hyperparameter λ . For $\lambda = 0.4$, the value of ENCE increases as opposite of the expected trend because the predicted value of the RMSE is larger than the value for RMV for most of the considered

bins. However, it is clear that for $\lambda \geq 0.5$, the ENCE is almost constant - which indicates that, on average, the model has a low probability to make incorrect predictions.

As a complement to the ENCE metric, the coefficient of variation (C_v) was also computed (red trace in Figure 3B). This metric is considered to be less informative because the dispersion of the prediction depends on the validation/test data distribution^{43,56}. However, it is useful to characterize the spread of standard deviations because it is desired that the predicted uncertainties are spread and therefore cover systems outside the training data which help to generalize the model and make it transferable to molecules outside the training set. Comparing the results from Figure 3A and the values for C_v in Figure 3B, it is found that the largest dispersion is obtained for small values of λ . This indicates that the standard deviations for all predictions are concentrated in a small range of values for values in the 95th percentile of the distribution. For $\lambda \geq 0.75$ both ENCE and C_v values do not show pronounced variation. It should be noted that the distributions in Figure 3A are restricted to the 99% quantile of the data; on the other hand, the values for C_v covered the whole range of data. If the complete range of data is analyzed, it is possible to arrive at wrong conclusions. Figure 3B shows that for $\lambda = 0.5$, the C_v value is large which suggests a flat distribution (Figure SIS2), however it should be noticed that this behaviour arises primarily due to pronounced outliers that impact the averages used for the calculation. However, 95% of the distribution is concentrated around a small range of variances as shown in Figure 3A. Nevertheless, if only 95% of the data is studied, it is found that $\lambda \geq 0.5$ yields increased C_v (see Figure S3).

From Figure 3A, it is observed a constant displacement of the center of mass of the distribution of predicted standard deviations. A more detailed analysis of the difference between Mean Squared Error and Mean Variance for different percentiles of the variance was performed (Figure S4 of the Supporting Information). Following the bias-variance decomposition of the squared error (Equation 15), the bias of the model can be quantified as a function of the different values of λ . Figure S4 shows that the MSE is constant regardless of the value of the hyperparameter λ or the percentile of the variance. On the other hand, the variance increases as a function of λ but it is constant regarding the value of the percentile with the exception of $\lambda = 1$. Thus, the MV is larger than the MSE which is

counter-intuitive in view of the bias-variance decomposition of the squared error. Finally, it is clear that the difference between MSE and MV decreases as the value of λ increases. This indicates that the assumed posterior distribution does not correctly describe the data and, as a consequence, it can not adequately capture the variance of a prediction. In other words, a better "guess" of the posterior will improve the predicted variance.

A common method to judge whether a model is well-calibrated is by considering the calibration curves described in the methods section. The results in Figure 4 show that, as λ increases, the model is closer to the diagonal which indicates perfect calibration. The best calibrated models are obtained for small values of λ ($\lambda = 0.1$ and $\lambda = 0.2$). Calibration curves help to evaluate the 'honesty' of the model predictions. Previously,⁵⁷ calibration curves were employed to select a suitable value for λ using the SchNet architecture⁵⁸ for QM9. These results largely agree with what is found here with $\lambda = 0.1$ and $\lambda = 0.2$ as the best values. Although calibration curves are extensively used in the literature to assess the quality of uncertainty predictions by ML models, they also have weaknesses that complicate their use. For example, it was reported⁴² that perfect calibration is possible for a model even if the output values are independent of the observed error. Furthermore, it was noticed⁴² that calibration curves work adequately when the uncertainty prediction is degenerate (i.e. all the output distributions have the same variance) which is not the desired behavior. In addition to this, it was found that the shape of these curves can be misleading because there are percentiles for which the model under- or overestimates the uncertainty. Then the calibration curves need to be complemented with additional metrics for putting their interpretation in perspective. Here, the analysis of calibration curves was complemented by using the miscalibration area (the area between the calibration curve and the diagonal representing perfect calibration). Using this metric, it is clear that λ values of 0.75 have a performance as good as $\lambda = 0.1$ and $\lambda = 0.2$.

B. Classification of Predictions

The effect of bias in the training set for PhysNet-type models was previously found to negatively impact prediction capabilities across chemical space.³² In the context of uncer-

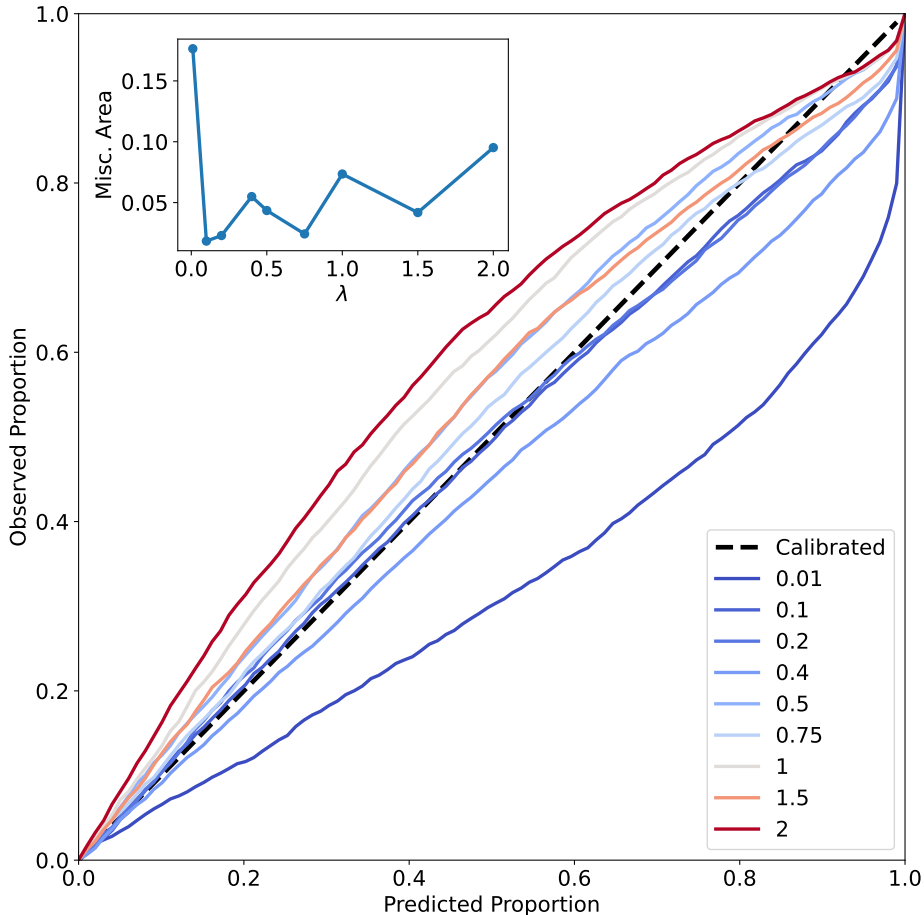


FIG. 4. Calibration curves with respect to the hyperparameter λ . The x-axis shows the predicted probability to obtain the correct value for the error in a given percentile, the y-axis shows the true probability. The trend line shows the behavior of a perfectly calibrated model. Inside the plot, the area between the curve and the trend line, also called Miscalibration Area, is shown as a function of the hyperparameter λ . A smaller miscalibration area indicates a better model.

tainty quantification, it is also of interest to understand how the predicted variance can be related to the error in the prediction for an individual prediction. For this, the relationship between the predicted variance and the error of prediction was studied following a classification scheme, see methods section. To this end, the subset of QM9 used for hyperparameter optimization was considered. Then the molecules in the test set were evaluated with the models trained with different values of the hyperparameter λ .

For all the tested models, the largest percentage of molecules ($\approx 80\%$) was found to be True

Negatives (TN), see Figure 5A. This indicates that the model can qualitatively correctly recognize for most of the samples that it has sufficient information to predict them correctly. On the other hand, the molecules classified as True Positives (TP) correspond to samples for which the model recognizes that they are difficult to predict. Hence, these molecules lie outside the training distribution because they present large errors on the prediction and the model is 'aware' of this. As expected, the number of TP and FP increases with the value of λ . This is a consequence of the inflation of the uncertainty by making the model less confident about its prediction which results in misclassification of molecules because as described before the error in the prediction is independent on the value of λ , see Figure SIS4. Finally, the number of False Negative (FN) samples in the data is approximately independent on λ . As described before, the molecules in this category contain information on the boundary of the training distribution which compromises the model's prediction capability. The constant number of FN is indicative of a systematic problem that can only be corrected by providing additional samples of similar molecules.

A summary of the relationship between the four classifications in term of model accuracy, sensitivity, and precision is given in Figure 5B. In all cases the accuracy of the model is appropriate, since the largest part ($\approx 90\%$) of the studied samples are correctly predicted (i.e. TN) and the variance reflects the prediction error. On the other hand, the precision of the model is also high ($\approx 80\%$) but starts to decrease as λ increases. In the present context, precision is a measure for the model's capability to recognize 'problematic' cases which also correspond to a real deficiency in the model which can be assessed by comparing the prediction with the true value and the predicted variance. It is expected that as the model becomes more underconfident, the precision decreases as there are more molecules misclassified due to inflation of the uncertainty. Conversely, sensitivity describes how many of the molecules that present a problem in the prediction are identified by the model. Here, the sensitivity increases for $\lambda > 0.5$: as the model becomes less confident, the probability to detect samples that are truly problematic increases. It should, however, also be pointed out that the numerical values for (ϵ^*, σ^*) to define the different categories will impact on how the classifications impact model characteristics such as "precision" or "sensitivity".

The MV and MSE for the complete set of samples as a function of λ are provided in Figure

5C. It is found that with the exception of $\lambda = 0.01$ and $\lambda = 0.5$, MV and MSE are comparable, which is a desired characteristic of the model. However, since it is additionally desirable that $MV < MSE$ the variance obtained by the model accounts for the variance term in equation 15. Therefore, the difference between MSE and MV is a constant value that corresponds to the combination of the bias of the model and the irreducible error. The advantage of this definition is that the variance can be mainly attributed to the data used for training. This provides a rational basis for further improvement of the training data. It is noted that the condition $MV < MSE$ is only fulfilled for $\lambda = 0.75$ and $\lambda > 1.5$. A summary with the values of all the metrics tested for calibration is given on Table S1 of supporting information.

Finally, the chemical structure of the molecules on the different categories is studied in Figure 5 D and Figures SIS5 - SIS8. Although the molecules used in the training, validation and test sets were kept constant for the different models, the molecules identified as outliers differed for each value of λ . However, it is instructive to identify the molecules that appear more frequently in the various tests. These chemical structures are studied in more detail on the following sections with the aim of identify systematic errors and sampling problems and how they can be corrected.

C. Artificial bias experiment

To provide a more chemically motivated analysis of predicted energies and associated variances, a model was trained using the first 25k molecules of QM9. The question addressed is whether predicted energies and variances for molecules not used in the training of the model are more likely to be true positives than for molecules with little coverage in the training set. Since the structures in QM9 were derived from graph enumeration, the order of the molecules in the database already biases certain chemical motifs, such as rings, chains, branched molecules and other features.

Figure 6A reports the Tree MAP (TMAP) projection⁵⁹ of the entire QM9 database (pink) and the first 25k molecules (blue). TMAP is a dimensionality reduction technique with good locality-preserving properties for high dimensional data such as molecular fingerprints.

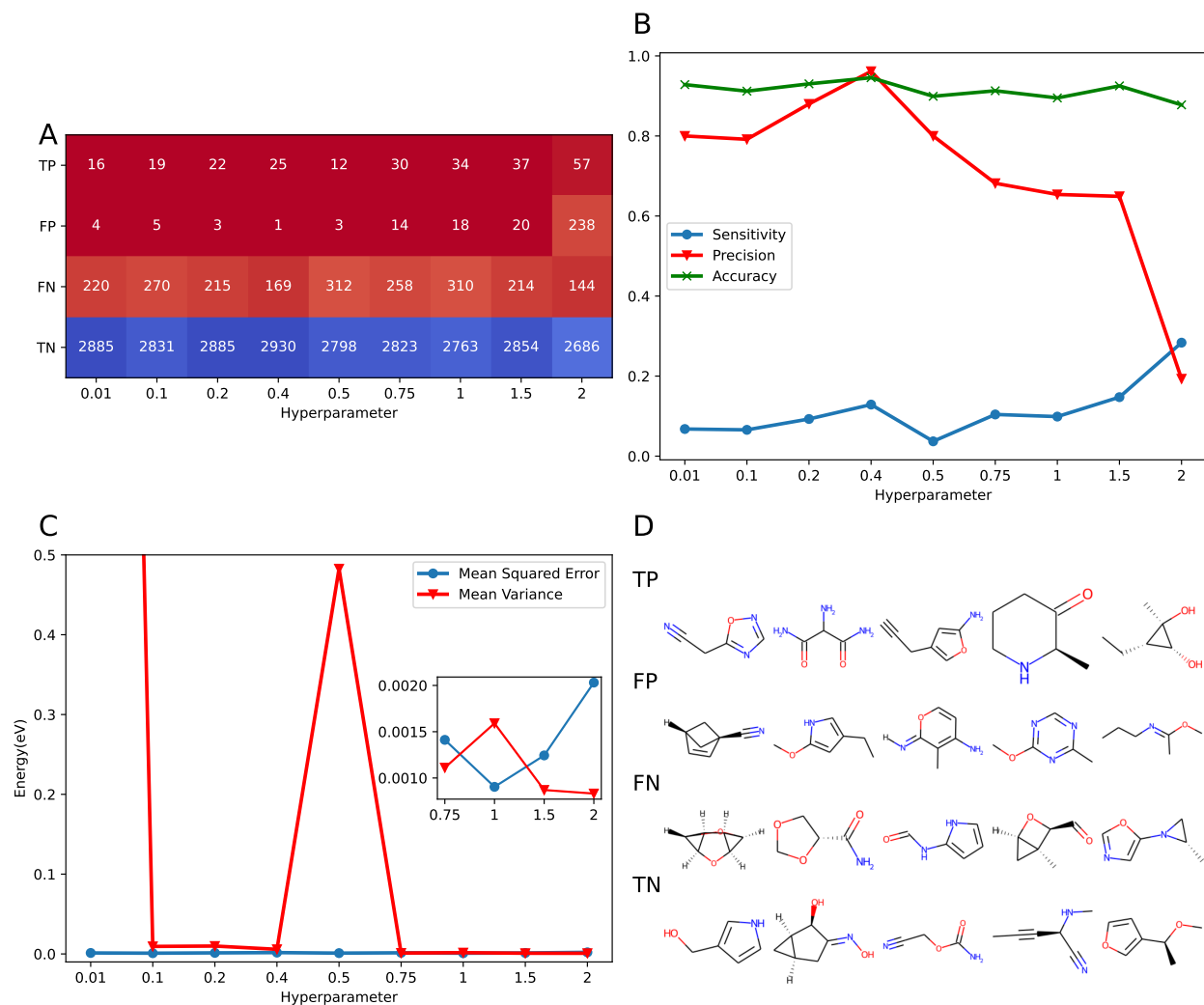


FIG. 5. Results of the classification procedure. **A.** Confusion matrix with respect to the value of the hyperparameter λ , inside each panel is the number of molecules that belong to the defined categories. The abbreviations refer to TP: True Positive, FP: False Positive, TN: True Negative, and FN: False Negative for information in how those categories are defined consult the methods section. **B.** Analysis of accuracy (Equation 16), sensitivity (Equation 17), and precision (Equation 18) for the different values of hyperparameter λ . **C.** The Mean Squared Error and Mean Variance for the full set of molecules as a function of the hyperparameter λ . The Mean Variance for $\lambda = 0.01$ is not shown for clarity. The inset of the plot shows the behavior for $\lambda \geq 0.75$. **D.** Chemical structures of the top 5 more common molecules in each of the described classes.

Analysis of the projection suggests that, as a general structural bias, the first 25k molecules over-represent aromatic heterocyclic, 5- and 6- membered rings, and structures with multiple substituted heteroatoms with regards to the relative probability of other structures also present in QM9.

For training the NN, as described in the methods section, 31500 structures were randomly split (train/validation/test of 0.8/0.1/0.1) and a model with $\lambda = 0.4$ was trained to make predictions on the test set. A TMAP projection of the test and train compounds is shown in Figure 6C. The connectivity of the different tree branches on the TMAP provides information about the local similarity of the molecules where dense regions of the map correspond to clusters of high similarity. The average degree i.e. number of edges between one molecule and its neighbors, for the TNs in the test set - which was the majority class ($\approx 90\%$ of the test samples) - was 2.0 compared with classes FN (169 molecules), TP (25 molecules), and FP (1 molecule) which had average degrees of 1.7, 1.3, 1.0. The lower connectivity (lower number of average neighbours in the minimum spanning tree) indicates that there is a rare molecule or it is not related to the main information used for training for FP compared with TN indicates that "good predictions for the right reason" are more likely if coverage of particular structural and/or chemical motifs is better. On the other hand, the different sample sizes of the four classes need to be kept in mind when generalizing such conclusions.

The TMAP projection of the test set in Figure 6B shows the chemical similarity between specific molecules seen during training or testing. In general, molecules identified as TPs contained common scaffolds seen during training in combination with unusual substituents. For example, the moiety of imidazole (a five-membered 1,3-C₃N₂ ring) was a common fragment in the training set and lies in the biased region of chemical space depicted in Figure 6A. Common true positives contained this imidazole scaffold inside uncommon fused three ring systems. When the model makes predictions on compounds close in chemical space to molecules of which it has seen diverse examples in the training set, the estimates of variance appear to be more reliable.

Figure 6D reports three examples of false positives (i.e. molecules with high error and low predicted variance) in the test set. The molecules in the training set are labelled as i, iii

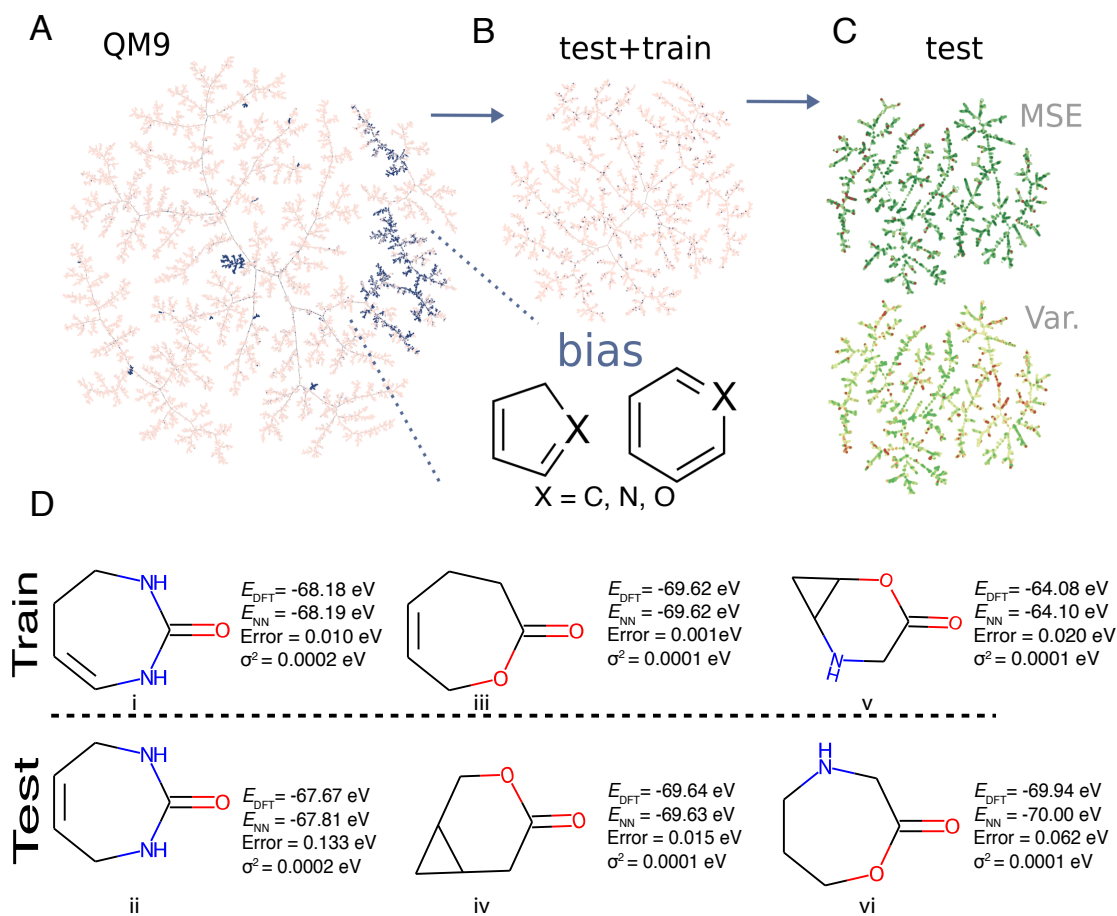


FIG. 6. Artificial bias experiment. **A** TMAP of the QM9 database. In blue the structures used for training, the inset shows that the selected part of the database bias the data towards specific chemistry, in this case, aromatic 6- and 5-membered heterocyclic rings scaffolds. In pink, the rest of the structures on QM9. **B** TMAP of the reduced dataset. In pink the structures used for training and validation and in blue the selected random compounds used for test. **C** TMAP of the test set. On top TMAP, for the MSE and down the corresponding for variance. The colormaps which span from the minimum value (green) to 1σ (red). **D** Pairs of similar molecules for which one molecule was in the training set (top) and the related molecule was in the test set (bottom) with reference, prediction and difference energies displayed together with associated variance.

and v, whereas those used for prediction from the test set were ii, iv and vi. The first pair, molecules i and ii, consist of a diazepane core that goes through a double bond migration. Although the rest of the structure is conserved between i and ii, the error in the prediction is of $\approx 0.1\text{eV}$, but the predicted variance is three orders of magnitude smaller. A possible explanation is that the model recognizes that it has similar information to the test molecule.

Therefore, it assigns a small variance; however, given that the difference in energy between those two molecules is of ≈ 0.5 eV, the model does not predict correctly molecule ii and overestimates its total energy.

Pair iii and iv present a more complicated case; here, the molecule used for training is an oxepane ring with a carbonyl. Meanwhile, we wish to predict an oxabicycloheptane. However, in this case, the model can predict the energy with an error of 0.01 eV. Therefore for pair iii and iv, the information that the model has from molecule iii, in addition to the significant presence of bicycles on the training set, makes easier the prediction of molecule iv. Finally, pair v and vi show the opposite case than pair iii and iv, starting with an Oxa-azabicycloheptane for predicting an Oxazepane. The error on this prediction is considerably higher, around 0.06 eV. This shows that the NN is more straightforward in predicting bicycles than seven-member rings. As mentioned, this is because there are more bicycles on the training set than seven-member rings; therefore, the interpolation to bicycles is easier for the model. An exciting aspect of all the molecules in Figure 6D is that all of them present the same number of heavy atoms, and they are largely similar in structure and bonding; therefore, for all of them, the model assigns a small variance because they resemble considerable to the information used for training.

Similarly, cases where a ring was expanded or contracted by a single atom between molecules in the training and test set commonly resulted in similar failure modes due to over-confidence. This observation is particularly interesting because it suggests that the model might be overconfident when predicting compounds it has seen sparse but highly similar examples of during training. Uncertainty quantification, in this conception, is effective at predicting in-distribution errors, however, out-of-distribution errors are not as easily quantified by this model.

D. Tautomerization set

As another application of how uncertainty quantification can be used, the prediction of energy of tautomer pairs was considered. Tautomerization is a form of reversible iso-

merization involving the rearrangement of a charged leaving group within a molecule.⁶⁰ The structures of the molecules involved in a tautomeric pair (A,B) only differ little which makes this an ideal application for the present developments. For the study of tautomeric pairs, three NN models with different values of $\lambda = 0.2, 0.4, 0.75$ were trained with QM9 database as described on the methods section. The test molecules considered come from the Tautobase database.⁵⁴ For the purpose of this work, only molecules with less than nine heavy atoms (C,N and O) were tested. A total of 442 pairs (884 molecules) were evaluated.

The training of PhysNet involves learning of the Atomic Embeddings (AE) and the centers and widths of the Radial Basis Functions (RBF). These features encode the chemical environment around each atom and therefore contain the "chemical information" about a molecule. This opens the possibility to further analyze the potential relationship contained in the learned parameters to the information about the chemical space contained in the training dataset and how it compares with the chemical space of the test molecules that are the target for prediction. Hence, for the following the mean distances between each of the tested molecules and the molecules in the training set of the database for $\langle \text{AE} \rangle$ and $\langle \text{RBF} \rangle$ were determined according to the procedure described in supporting information, see SI Section S1. Figure 7 shows the results for the relationships between the mean distance of the AE and RBF, the error, variance and number of atoms for the molecules on the tautobase.

The bottom row of Figure 7A (panels i to v) report $\langle \text{AE} \rangle$ and $\langle \text{RBF} \rangle$, the prediction errors and associated variances sorted by the number of heavy atoms $N = 3$ to 9 together with the distribution $P(N)$. The dependence of $\langle \text{AE} \rangle$ and $\langle \text{RBF} \rangle$ on N shows that with decreasing number of heavy atoms the mean distance with respect to the molecules with the same number of atoms increases (Figure 7A i and ii). Additionally, the violin plots in Figure 7A i and ii show that the mean distance values are more spread as the number of atoms increases. A possible explanation for these results is that the possible chemical space to explore increases with N which is also reflected in the number of samples with a given number of heavy atoms on the training dataset; consequently, the distance between the molecules with a low number of atoms increases. In other words, a larger molecule allows a more extensive chemical space to explore in terms of chemical environments, atom types, bonding patterns and other characteristics of chemical space. The relationship between error and

the number of atoms illustrates how the smaller mean distance on RBF and AE gives place to a smaller error. However, the distribution for error is less sparsely distributed for smaller molecules as the same happens with the distances for the features of the model (Figure 7A iii). Comparing error and variance by the number of heavy atoms, it is clear that up to 5 atoms, the tendency for both are the same (Figure 7A xiv) . From Figure 7A iii, it is clear that the error on distribution shifts when the number of atoms in the molecule increases. For the case of the predicted variance (Figure 7A iv) the distribution has a center of mass at a high value and progressively decreases until 5 heavy atoms to increase again. It should be noted that the number of outliers for error and variance increases with the number of heavy atoms, therefore the displacement on the center of mass of the distribution can be overestimated by the presence of them. Finally, the spread of error and variance by the number of atoms (Figure 7A iii and iv) presents similar shapes up to 8 heavy atoms. For the molecules with 8 and 9 atoms, the values of the variance are more spread meanwhile the error distribution is more compact.

Panels vi, vii, x, and xi in Figure 7A show that variance and error are similarly distributed depending on $\langle \text{AE} \rangle$ and $\langle \text{RBF} \rangle$, respectively. For the entire range of $\langle \text{AE} \rangle$ and $\langle \text{RBF} \rangle$ low variance (< 0.0002 eV) and low prediction errors (< 0.25 eV) are found. Increased variance (~ 0.0005 eV) is associated with both, larger $\langle \text{AE} \rangle$ and $\langle \text{RBF} \rangle$ whereas larger prediction errors (> 1.0 eV) are found for intermediate to large $1.0 \leq \langle \text{RBF} \rangle \leq 1.5$. This similarity is also reflected in a near-linear relationship between $\langle \text{AE} \rangle$ and $\langle \text{RBF} \rangle$ reported in panel xiii of Figure 7A.

Prediction error and variance are less well correlated for the evaluated molecules from tautobase, see panel viii of Figure 7A. This can already be anticipated when comparing panels i and ii. With increasing N , the position of the maximum error shifts monotonously to larger values whereas the variance is higher for $N = 3$, decreases until $N = 6$, after which it increases again. Hence, for tautobase and QM9 as the reference data, base error and variance are not necessarily correlated.

To gain a better understanding of the performance of QM9 on the prediction of the molecules in the Tautobase from the point of view of the feature space, polar plots considering extreme

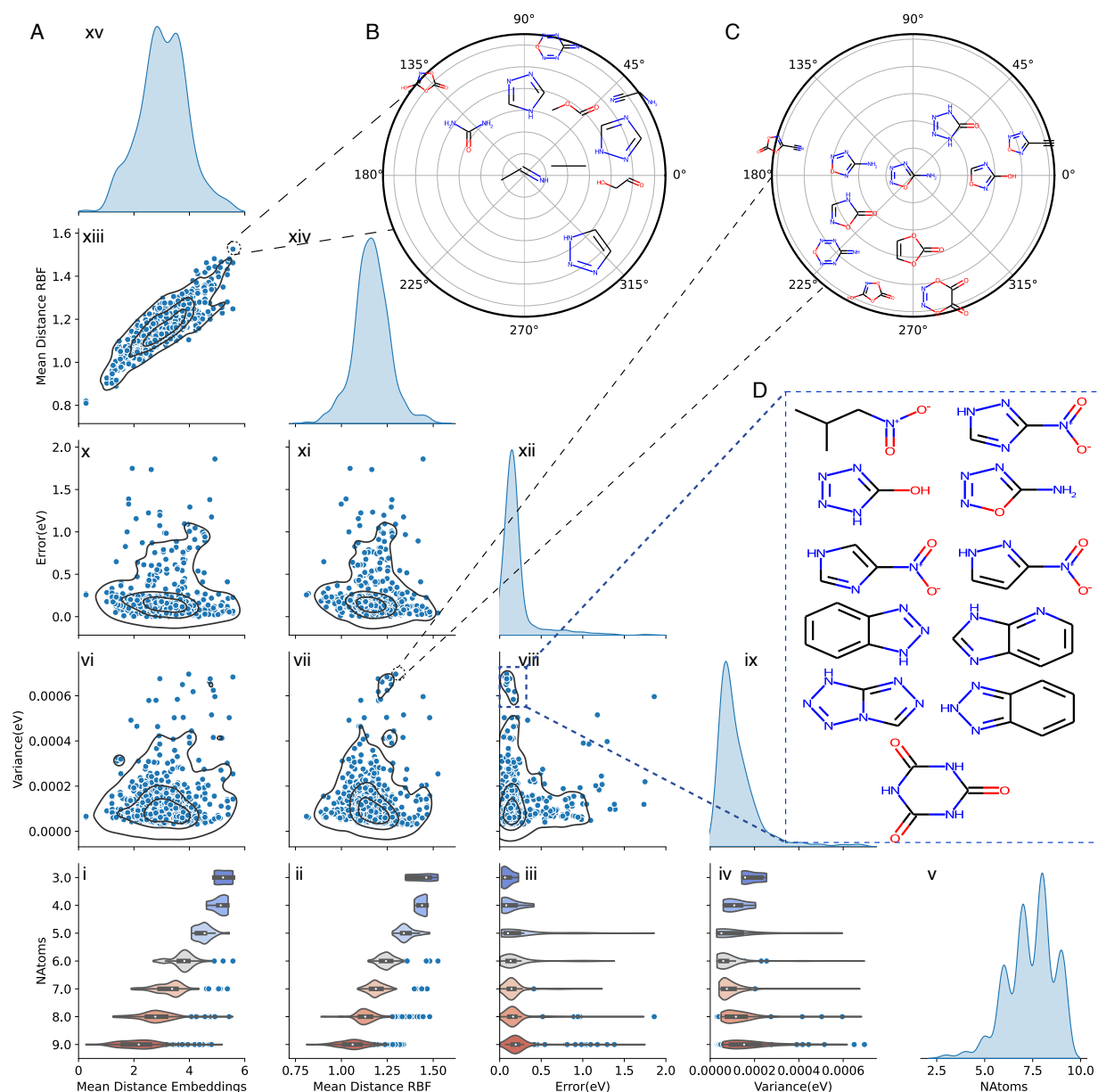


FIG. 7. **A** Overview of the comparison between different results for the evaluation of molecules on the tautobase for $\lambda = 0.75$ up to the 95th percentile. The diagonal of the figure shows the kernel density estimate of the considered properties (Mean Distance Embeddings, Mean Distance RBF, Error (in eV), Variance (in eV) and Number of Atoms). For each of the panels a correlation plot between the variable and a 2D kernel density estimate is shown. On the last row, violin plots for the different considered properties with respect to the number of atoms is shown. Similar plots for $\lambda = 0.2$ and $\lambda = 0.4$ can be found on the Supporting Information. **B** Radial plot of the ten closest molecules of the training set on feature space for the molecule in tautobase with the largest distance in embedding and RBF space. **C** Radial plot of the ten closest molecules for the molecule in tautobase with the largest predicted variance and the largest distance in RBF space. **D** Examples of molecules with large predicted variance and small error.

cases were constructed. Figure 7B shows the case for the molecule (center) with the largest mean distance in RBF and embedding space for the molecules with the same number of atoms used for training for this representation; only the ten closest neighbours are shown. It is clear that although the molecule is relatively simple, no structure contains information for its prediction. The influence of 'noise' in the sense of molecules with similar chemical environments but bond to other functional groups is observed. Another case is shown in panel C of figure 7 where the molecule with the largest variance and largest distance on the RBF space is shown. This case is similar to what was previously observed for molecule ii on figure 6D, where a simple change in the geometry gives place to large values. However, for this case, we observe that the presence of many similar structures on the training set makes the model give a large estimate of the variance because of all the similar structural information available for the prediction. The influence of redundant data was previously observed³² where the ANI-1 database gives less accurate results than the ANI-1E database for the influence of redundant information that makes the fitting procedure more complicated. As a final example of the relationship between error and variance, the chemical structures for a set of molecules with low error but the high variance is highlighted in figure 7D. We observe the presence of heterocyclic rings and bicycles, which are well represented on the training set. An interesting aspect is that the functional group nitro is present in many molecules with a high variance and a low error. The effect of the nitro functional group can be understood from the design of the GDB-17 Database⁶¹ which is the source of the QM9 database; for GDB-17 aliphatic nitro groups were excluded, but aromatic nitro groups were kept. Therefore, the model will have similar but not good information about this functional group, giving place to significant variances.

Finally, it is of interest to analyze tautomer pairs (A/B) for which the difference in the predicted variance is particularly large, see Figure 8A, where the distribution $p(\sigma_A^2 - \sigma_B^2)$ is shown for trained models with different values of the hyperparameter λ . Large differences (star in Figure 8A) in the variances indicate that the trained models are particularly uncertain in its predictions. Four tautomer pairs were identified to which this applies and are analyzed in more detail here. For molecules B1 to B3 it is found that their functional groups are not present in QM9, such as the N=O nitro group in a aliphatic chain (B1), vinyl alcohol (B2), or hydroxyl imine (B3, only one representative in QM9). The pair (A1,B1) is

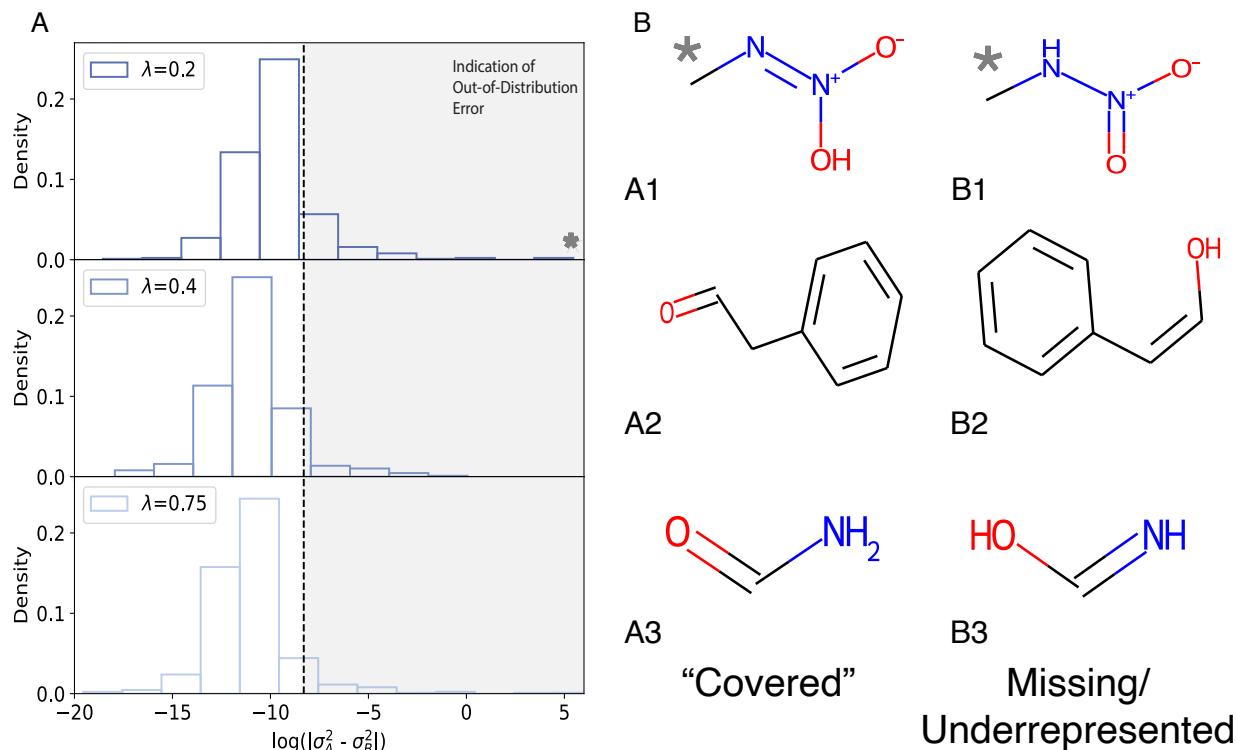


FIG. 8. **A** The log distribution of differences in predicted variance between tautomer pairs, A (low variance) and B (high variance). **B** Tautomer pairs (A/B) containing chemical groups, nitro and vinyl alcohols, outside the training set (B1-3) are easily identified. The imine group in B3 was identified in only one molecule in the training set. Energy values: A1: $E_{\text{DFT}} = -30.86\text{eV}$, $E_{\text{NN}} = (-32.67, -32.58, -32.20)\text{eV}$, $\sigma^2 = (0.0457, 0.0004, 0.2243)\text{eV}$, B1: $E_{\text{DFT}} = -31.63\text{eV}$, $E_{\text{NN}} = (-32.02, -32.08, -32.69)\text{eV}$, $\sigma^2 = (229.62, 0.0035, 0.0033)\text{eV}$. A2: $E_{\text{DFT}} = -79.89\text{eV}$, $E_{\text{NN}} = (-79.68, -79.69, -79.68)\text{eV}$, $\sigma^2 = (0.0018, 0.0002, 0.0002)\text{eV}$, B2: $E_{\text{DFT}} = -79.59\text{eV}$, $E_{\text{NN}} = (-79.28, -79.44, -79.36)\text{eV}$, $\sigma^2 = (0.0249, 0.0002, 0.0003)\text{eV}$ A3: $E_{\text{DFT}} = -23.59\text{eV}$, $E_{\text{NN}} = (-23.52, -23.52, -23.52)\text{eV}$, $\sigma^2 = (0.0016, 0.0012, 0.0002)\text{eV}$ B3: $E_{\text{DFT}} = -23.02\text{eV}$, $E_{\text{NN}} = (-22.75, -22.88, -22.91)\text{eV}$, $\sigma^2 = (0.0019, 0.0011, 0.0007)\text{eV}$

zwitterionic.

As shown in Figure 8B the chemical motifs and functional groups in the representatives A1 to A3 are covered by QM9 whereas those in their tautomeric twins (B1 to B3) are not. For B1 to B3 the predicted variances are particularly large and the reasons for this can be directly linked to the chemical structures covered by QM9. For B1 some of the atom-atom

separations (“bond lengths”) are outside those covered by QM9. For the N–N distance, the QM9 database covers 1.2 to 1.4 Å whereas N–N in B1 is 1.383 Å (See figure SIS14). In the case of B1, QM9 only contains few examples of sp^2 NO bonds except for a small number of hetrocyclic rings which are chemically dissimilar compound B1. For molecule B2 vinyl alcohols are absent from QM9 and the presence of hydroxyl groups bound to sp^2 carbons is not sufficient for a reliable prediction for B2. And for B3 only one molecule with an imine group is in QM9 which is the reason for the uncertainty in the prediction.

IV. CONCLUSIONS

This work introduces uncertainty quantification for the prediction of total energies and variances for molecules based on a trained neural network. The architecture chosen is that of PhysNet but it is anticipated that the main ideas can be transferred to other architectures as well. An earlier study applied uncertainty quantification to molecular discovery and inference for virtual screening and discussed the advantages for prioritization.⁵⁷ Essential findings of the present work concern the notion that single metrics are not particularly meaningful to judge the calibration of a trained model. Exploration and development of meaningful metrics will benefit evidence-based inference. Also, it is not always true that error and variance are directly related which is counter typical expectations in statistical learning. For such findings uncertainty quantification is essential and reveals that the nature and coverage of the training set used for model construction plays an important role. It is also demonstrated that mean variance and mean squared error can behave in counter-intuitive ways which points towards deficiencies in the assumed posterior distribution. Finally, it is demonstrated for the case of tautomerization energies that classification of predictions can be used to isolate problematic cases at the prediction stage. These shortcomings can be linked to missing or poor coverage in the training data set. Considering the mean distance in feature space, it was found that information needs to be added in a rational fashion because the presence of too much redundant information destabilizes the model. This can be seen, e.g., in that large variances are assigned to molecules that are otherwise correctly predicted. Similar information in low quantities returns low uncertainties but high errors, similar information in large quantities results in small errors but high predicted uncertain-

ties. A notable example of this is the nitro group in the training database, which is excluded from aliphatic chains but is found in aromatic rings. Thus, for a balanced ML-based model for chemical exploration an equilibrium between the quantity and the quality of the data in the database is required. This information can be used in the future to build targeted and evidence-based databases for a broad range of chemical observables based on active learning strategies and for constructing high-dimensional potential energy surfaces of molecules.

ACKNOWLEDGMENTS

The authors acknowledge financial support from the Swiss National Science Foundation (NCCR-MUST and Grant No. 200021-7117810, to MM) and the University of Basel. LIVS acknowledges fruitful discussions with Dr. Kai Töpfer and Dr. Oliver Unke.

REFERENCES

- ¹M. Meuwly, Chem. Rev. **121**, 10218 (2021).
- ²K. Töpfer, S. Käser, and M. Meuwly, Physical Chemistry Chemical Physics (2022).
- ³F. Noé, S. Olsson, J. Köhler, and H. Wu, Science **365**, eaaw1147 (2019).
- ⁴S. Manzhos and T. Carrington Jr, Chem. Rev. **121**, 10187 (2020).
- ⁵D. Koner and M. Meuwly, J. Chem. Theory Comput. **16**, 5474 (2020).
- ⁶R. Conte, C. Qu, P. L. Houston, and J. M. Bowman, J. Chem. Theory Comput. **16**, 3264 (2020).
- ⁷O. T. Unke, S. Chmiela, H. E. Sauceda, M. Gastegger, I. Poltavsky, K. T. Schütt, A. Tkatchenko, and K.-R. Müller, Chem. Rev. **121**, 10142 (2021).
- ⁸O. T. Unke, M. Stöhr, S. Ganscha, T. Unterthiner, H. Maennel, S. Kashubin, D. Ahlin, M. Gastegger, L. M. Sandonas, A. Tkatchenko, *et al.*, arXiv preprint arXiv:2205.08306 (2022).
- ⁹D. Schwalbe-Koda and R. Gómez-Bombarelli, in *Machine Learning Meets Quantum Physics* (Springer, 2020) pp. 445–467.
- ¹⁰B. Huang and O. A. von Lilienfeld, Chem. Rev. **121**, 10001 (2021).

- ¹¹K. T. Schütt, H. E. Saucedo, P.-J. Kindermans, A. Tkatchenko, and K.-R. Müller, J. Chem. Phys. **148**, 241722 (2018).
- ¹²J. S. Smith, O. Isayev, and A. E. Roitberg, Chem. Sci. **8**, 3192 (2017).
- ¹³X. Gao, F. Ramezanghorbani, O. Isayev, J. S. Smith, and A. E. Roitberg, J. Chem. Inf. Model. **60**, 3408 (2020).
- ¹⁴T. W. Ko, J. A. Finkler, S. Goedecker, and J. Behler, Nat. Comm. **12**, 1 (2021).
- ¹⁵O. T. Unke, S. Chmiela, M. Gastegger, K. T. Schütt, H. E. Saucedo, and K.-R. Müller, Nat. Comm. **12**, 1 (2021).
- ¹⁶J. A. Keith, V. Vassilev-Galindo, B. Cheng, S. Chmiela, M. Gastegger, K.-R. Müller, and A. Tkatchenko, Chem. Rev. **121**, 9816 (2021).
- ¹⁷P. Domingos, Communications of the ACM **55**, 78 (2012).
- ¹⁸H. Sanders and J. Saxe, Proceedings of Blackhat **2017** (2017).
- ¹⁹M. F. Kilkenny and K. M. Robinson, Health Information Management Journal **47**, 103 (2018).
- ²⁰G. Canbek, Wiley Interdisciplinary Reviews: Data Mining and Knowledge Discovery **12**, e1456 (2022).
- ²¹R. L. Tweedie, K. L. Mengersen, and J. A. Eccleston, Chance **7**, 20 (1994).
- ²²C. Babbage, *Passages from the Life of a Philosopher*, Cambridge Library Collection - Technology (Cambridge University Press, 2011).
- ²³R. S. Geiger, D. Cope, J. Ip, M. Lotosh, A. Shah, J. Weng, and R. Tang, Quantitative Science Studies **2**, 795 (2021).
- ²⁴J. C. Weyerer and P. F. Langer, in *Proceedings of the 20th Annual International Conference on Digital Government Research* (2019) pp. 509–511.
- ²⁵B. Saha and D. Srivastava, in *2014 IEEE 30th international conference on data engineering* (IEEE, 2014) pp. 1294–1297.
- ²⁶F. Iafrate, in *Digital Enterprise Design & Management* (Springer, 2014) pp. 25–33.
- ²⁷M. T. Baldassarre, I. Caballero, D. Caivano, B. Rivas Garcia, and M. Piattini, in *Proceedings of the 1st ACM SIGSOFT International Workshop on Ensemble-Based Software Engineering* (2018) pp. 19–24.
- ²⁸I. Triguero, D. García-Gil, J. Maillo, J. Luengo, S. García, and F. Herrera, Wiley Interdisciplinary Reviews: Data Mining and Knowledge Discovery **9**, e1289 (2019).
- ²⁹O. A. Von Lilienfeld, Angew. Chem. Int. Ed. **57**, 4164 (2018).

- ³⁰S. Heinen, M. Schwilk, G. F. von Rudorff, and O. A. von Lilienfeld, Mach. Learn.: Sci. Technol. **1**, 025002 (2020).
- ³¹S. Käser, D. Koner, A. S. Christensen, O. A. von Lilienfeld, and M. Meuwly, J. Phys. Chem. A **124**, 8853 (2020).
- ³²L. I. Vazquez-Salazar, E. D. Boittier, O. T. Unke, and M. Meuwly, J. Chem. Theory Comput. **17**, 4769 (2021).
- ³³S. Käser, O. T. Unke, and M. Meuwly, New J. Phys. **22**, 055002 (2020).
- ³⁴J. P. Janet, C. Duan, T. Yang, A. Nandy, and H. J. Kulik, Chem. Sci. **10**, 7913 (2019).
- ³⁵P. Zheng, W. Yang, W. Wu, O. Isayev, and P. O. Dral, J. Phys. Chem. Lett. **13**, 3479 (2022).
- ³⁶J. Gawlikowski, C. R. N. Tassi, M. Ali, J. Lee, M. Humt, J. Feng, A. Kruspe, R. Triebel, P. Jung, R. Roscher, *et al.*, arXiv preprint arXiv:2107.03342 (2021).
- ³⁷M. Abdar, F. Pourpanah, S. Hussain, D. Rezazadegan, L. Liu, M. Ghavamzadeh, P. Fieguth, X. Cao, A. Khosravi, U. R. Acharya, *et al.*, Information Fusion **76**, 243 (2021).
- ³⁸A. Amini, W. Schwarting, A. Soleimany, and D. Rus, in *Advances in Neural Information Processing Systems*, Vol. 33, edited by H. Larochelle, M. Ranzato, R. Hadsell, M. F. Balcan, and H. Lin (Curran Associates, Inc., 2020) pp. 14927–14937.
- ³⁹O. T. Unke and M. Meuwly, J. Chem. Theory Comput. **15**, 3678 (2019).
- ⁴⁰A. Paszke, S. Gross, F. Massa, A. Lerer, J. Bradbury, G. Chanan, T. Killeen, Z. Lin, N. Gimeshein, L. Antiga, A. Desmaison, A. Kopf, E. Yang, Z. DeVito, M. Raison, A. Tejani, S. Chilamkurthy, B. Steiner, L. Fang, J. Bai, and S. Chintala, in *Advances in Neural Information Processing Systems 32* (2019) pp. 8024–8035.
- ⁴¹D. P. Kingma and J. Ba, arXiv preprint arXiv:1412.6980 (2014).
- ⁴²D. Levi, L. Gispán, N. Giladi, and E. Fetaya, arXiv preprint arXiv:1905.11659 (2019).
- ⁴³K. Tran, W. Neiswanger, J. Yoon, Q. Zhang, E. Xing, and Z. W. Ulissi, Mach. Learn.: Sci. Technol. **1**, 025006 (2020).
- ⁴⁴J. Busk, P. B. Jørgensen, A. Bhowmik, M. N. Schmidt, O. Winther, and T. Vegge, Mach. Learn.: Sci. Technol. **3**, 015012 (2021).
- ⁴⁵V. Kuleshov, N. Fenner, and S. Ermon, in *International conference on machine learning* (PMLR, 2018) pp. 2796–2804.
- ⁴⁶Y. Chung, I. Char, H. Guo, J. Schneider, and W. Neiswanger, arXiv preprint arXiv:2109.10254 (2021).

- ⁴⁷P. Pernot, J. Chem. Phys. **156**, 114109 (2022).
- ⁴⁸L. Kahle and F. Zipoli, Phys. Rev. E **105**, 015311 (2022).
- ⁴⁹K. Cheng, F. Calivá, R. Shah, M. Han, S. Majumdar, and V. Pedoia, in *Medical Imaging with Deep Learning* (PMLR, 2020) pp. 121–135.
- ⁵⁰T. Hastie, R. Tibshirani, J. H. Friedman, and J. H. Friedman, *The elements of statistical learning: data mining, inference, and prediction* (Springer, 2009).
- ⁵¹M. J. Schervish and M. H. DeGroot, *Probability and statistics* (Pearson Education London, UK:, 2014).
- ⁵²J. Watt, R. Borhani, and A. K. Katsaggelos, *Machine learning refined: Foundations, algorithms, and applications* (Cambridge University Press, 2020).
- ⁵³O. Wahl and T. Sander, J. Chem. Inf. Model. **60**, 1085 (2020).
- ⁵⁴L. I. Vazquez-Salazar and M. Meuwly, “Qtautobase: A quantum tautomerization database,” (2021).
- ⁵⁵B. Ruscic, Int. J. Quantum Chem. **114**, 1097 (2014).
- ⁵⁶G. Scalia, C. A. Grambow, B. Pernici, Y.-P. Li, and W. H. Green, J. Chem. Inf. Model. **60**, 2697 (2020).
- ⁵⁷A. P. Soleimany, A. Amini, S. Goldman, D. Rus, S. N. Bhatia, and C. W. Coley, ACS Cent. Sci. **7**, 1356 (2021).
- ⁵⁸K. Schutt, P. Kessel, M. Gastegger, K. Nicoli, A. Tkatchenko, and K.-R. Müller, J. Chem. Theory Comput. **15**, 448 (2018).
- ⁵⁹D. Probst and J.-L. Reymond, J. Cheminf. **12**, 12 (2020).
- ⁶⁰A. Wilkinson and A. McNaught, International Union of Pure and Applied Chemistry: Zürich, Switzerland (1997).
- ⁶¹L. Ruddigkeit, R. Van Deursen, L. C. Blum, and J.-L. Reymond, J. Chem. Inf. Model. **52**, 2864 (2012).
- ⁶²R. Ramakrishnan, P. O. Dral, M. Rupp, and O. A. Von Lilienfeld, Sci. Data **1**, 140022 (2014).

Supporting Information: Uncertainty quantification for predictions of atomistic neural networks

S1. CALCULATION OF THE MEAN DISTANCE BETWEEN TRAINING AND TEST MOLECULES IN FEATURE SPACE.

The mean distance between the molecules from the tautobase and the molecules in QM9 was calculated as follows. First, for each of the molecules in the test set, the molecules with the same number of atoms in the tautobase were filtered. This because the size of the matrices of Radial Base Functions and embedding need to be of the same size. In the second step, the pairwise distance between the test molecule and the filtered molecules was calculated using the Euclidean norm between points as:

$$||X||_i = \frac{1}{n} \sqrt{\sum_{j=1}^n \sum_{k=1}^n (x_j - y_k^i)^2} \quad (19)$$

where x_j is the element in the RBF/embedding matrix of the test molecule, y_k^i is the element in the RBF/embedding matrix for each of the filter molecules and n is the elements on the RBF matrix/embedding matrix. Therefore the value obtained from equation 19 is the mean distance between the RBF/embedding matrix of the test molecule and the i th-molecule on the training dataset.

In the next step, the distance between each of the molecules with the same size and the test molecule is average to obtain the average distance in feature space between the target molecule and the molecules with the same number of atoms in embedding space as:

$$\langle \text{RBF/AE} \rangle = \frac{1}{N} \sum_{i=1}^N ||X||_i \quad (20)$$

A. Construction of polar plots

The polar plots drawn in figure 7B,C and in figures S11-S13 represent a projection of the distance between a test molecule(center) and the close molecules in embedding space. The value for $||AE||$ and $||RBF||$ between the test molecule and the molecule in the training dataset obtained from 19 are transformed to polar values according to the following

expressions:

$$r = \sqrt{||AE||^2 + ||RBF||^2} \quad (21)$$

$$\theta = \arctan \frac{||AE||}{||RBF||} \quad (22)$$

S2. TABLES

λ	Calibration	MSE	MV	Sharpness	Dispersion	ENCE	C_v	MA	Sensitivity	Precision	Accuracy
0.01	Poor	0.0012	3.3895	0.0078	0.5500	0.1930	1.3041	0.1765	0.0678	0.8000	0.9283
0.1	Poor	0.0009	0.0094	0.0133	0.4400	0.1465	0.3196	0.0184	0.0657	0.7917	0.9120
0.2	Regular	0.0013	0.0099	0.0137	0.5700	0.1416	0.3080	0.0229	0.0928	0.8800	0.9302
0.4	Good	0.0017	0.0058	0.0113	0.4500	0.1422	0.6542	0.0549	0.1289	0.9615	0.9456
0.5	Poor	0.0010	0.4827	0.0189	0.5800	0.1383	0.1775	0.0435	0.0370	0.8000	0.8992
0.75	Good	0.0014	0.0011	0.0179	0.5100	0.1545	0.2554	0.0242	0.1042	0.6818	0.9130
1	Poor	0.0009	0.0016	0.0196	0.4700	0.1649	0.2020	0.0735	0.0988	0.6538	0.8950
1.5	Regular	0.0012	0.0009	0.0165	0.3800	0.1551	0.2357	0.0418	0.1474	0.6491	0.9251
2	Poor	0.0020	0.0008	0.0220	0.1500	0.1684	0.2542	0.0952	0.2836	0.1932	0.8778

TABLE S1. Summary of the properties tested for calibration of the evaluated models. Units when necessary are in eV. MSE: Mean Square Error, MV: Mean Variance, ENCE: Expected Normalized Calibration Error, MA: Miscalibration Area.

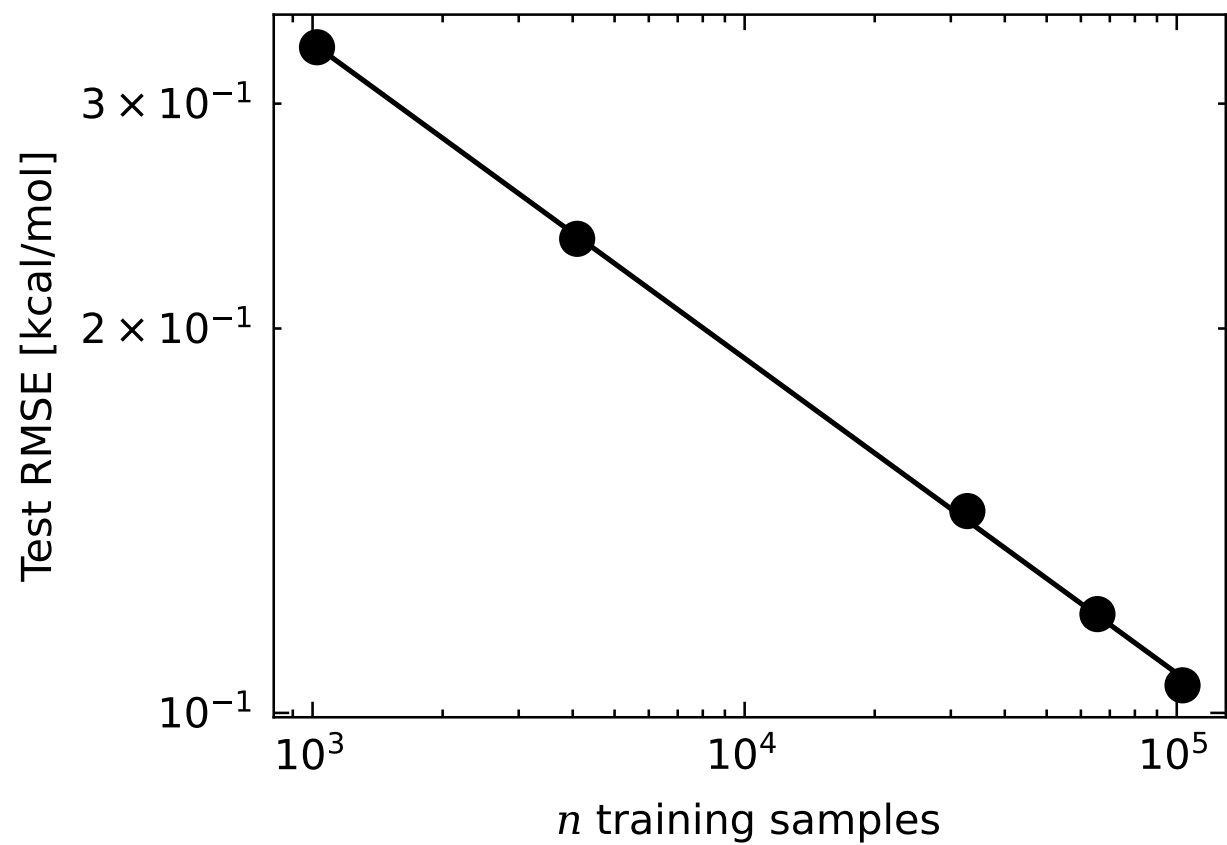


FIG. S1. Learning curves showing the improvement of model with respect to training set size.

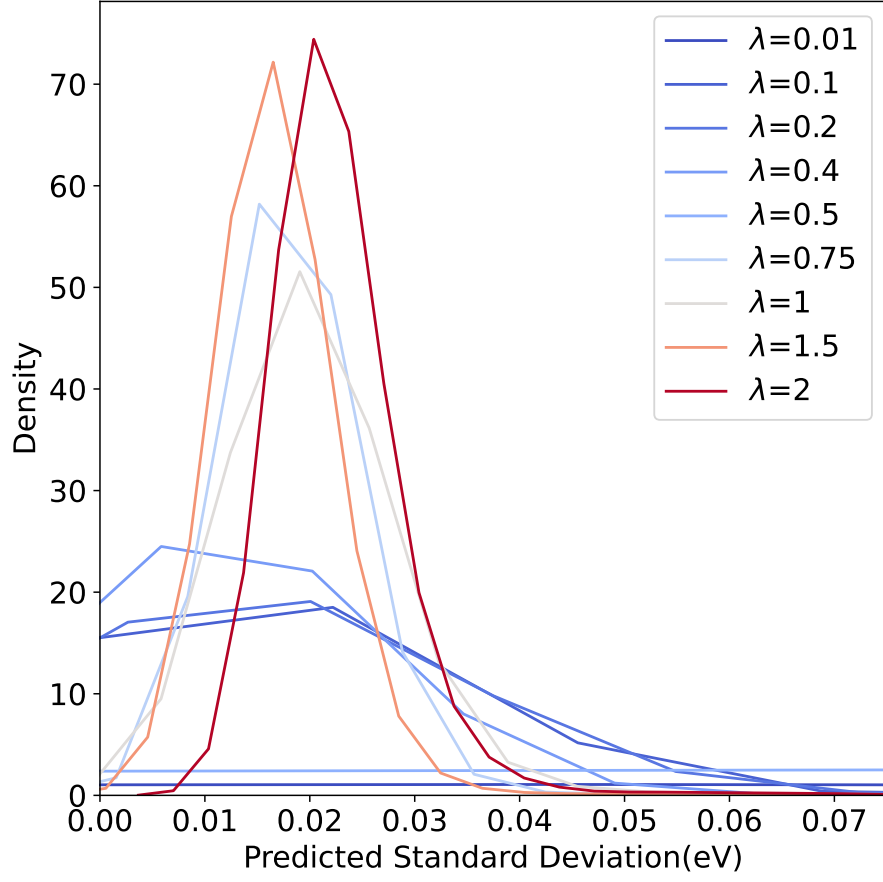


FIG. S2. Distribution of standard deviation($\sigma = \sqrt{Var}$) for different values of hyperparameter λ . All the values were considered.

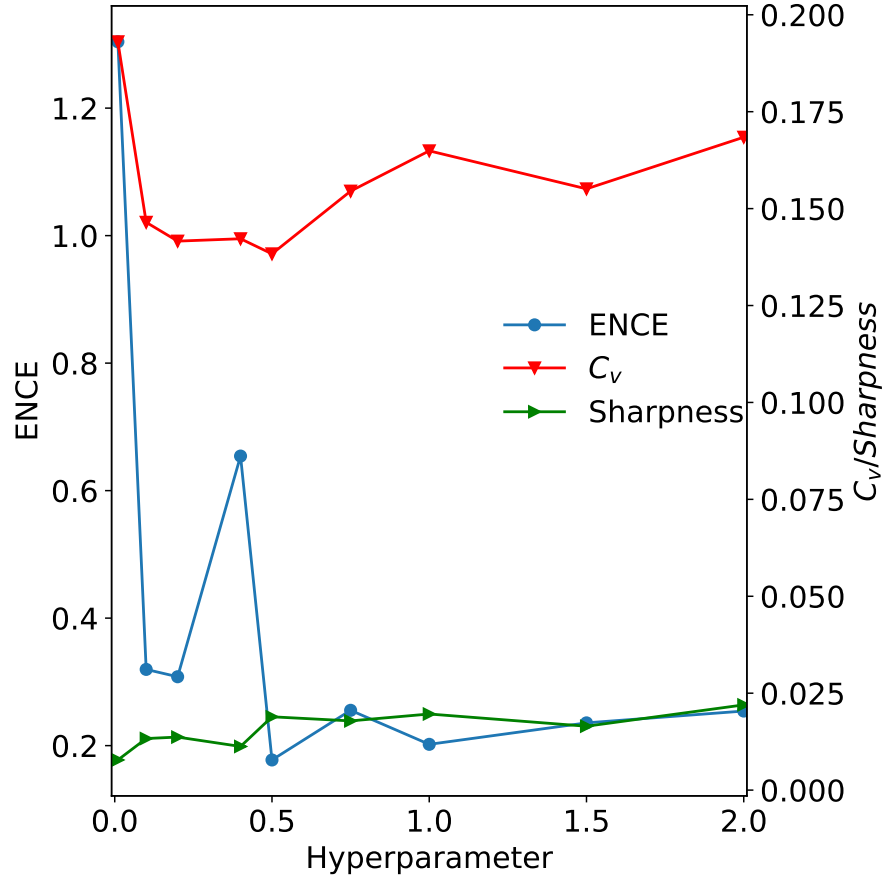


FIG. S3. Evolution of the Expected Normalized Calibration Error (ENCE), sharpness, and the Coefficient of Variation (C_v) depending on λ for the 95% of the variance distribution

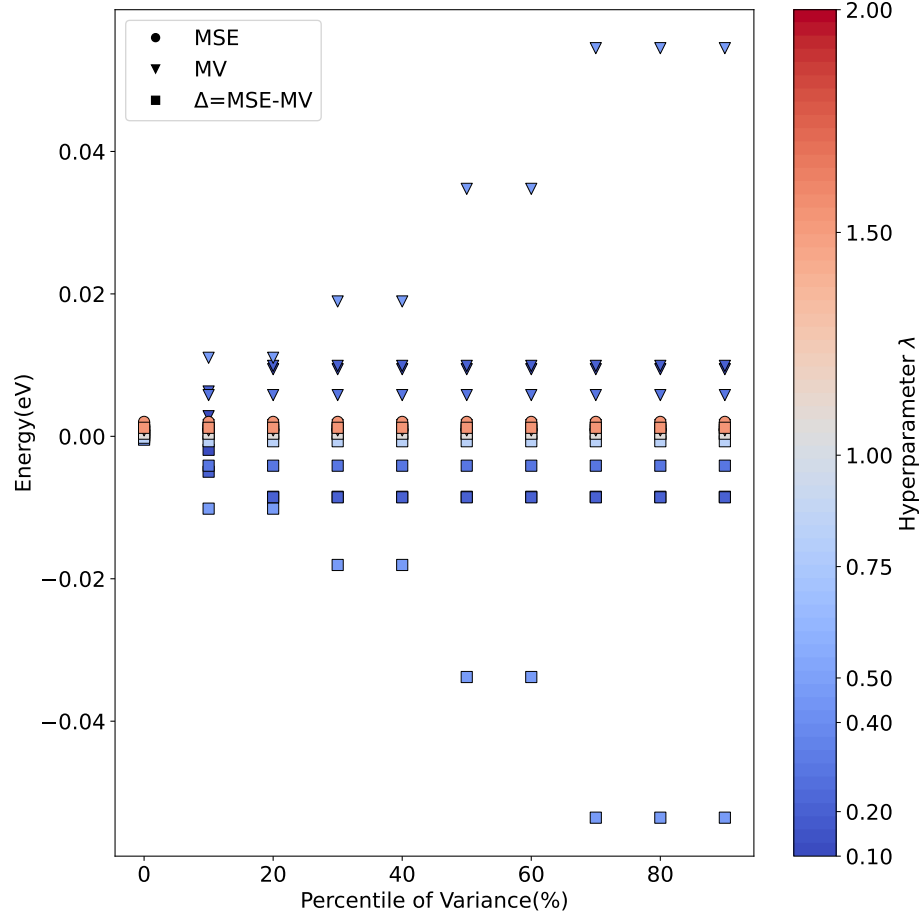


FIG. S4. Difference between Mean Squared Error (MSE) and Mean Variance (MV) for different percentiles of the predicted variance. Values for MSE, MV and its difference (Δ) at a given quantile are shown with different labels. The color bar indicates the values of the hyperparameter λ . The different dots are colored accordingly to its λ value. Value for 0.01 was excluded for clarity.

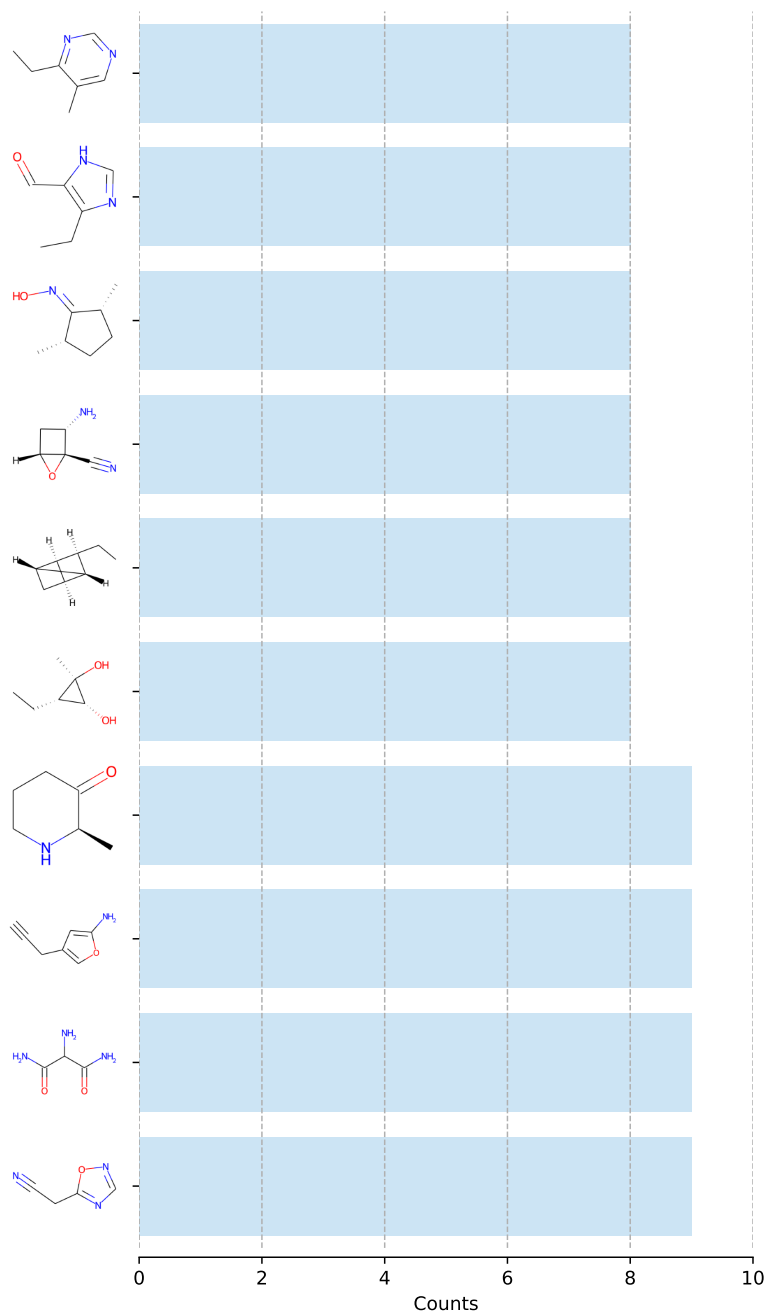


FIG. S5. Top 10 Common True Positive (TP) molecules ($\varepsilon_i > \varepsilon_{max}$ and $\sigma_i > \sigma_{max}$). The x-axis shows how often a molecule appear as TP for the different values of hyperparameter λ , the y-axis show the characteristic chemical structure. There are only show molecules that appear for at least four different values of λ

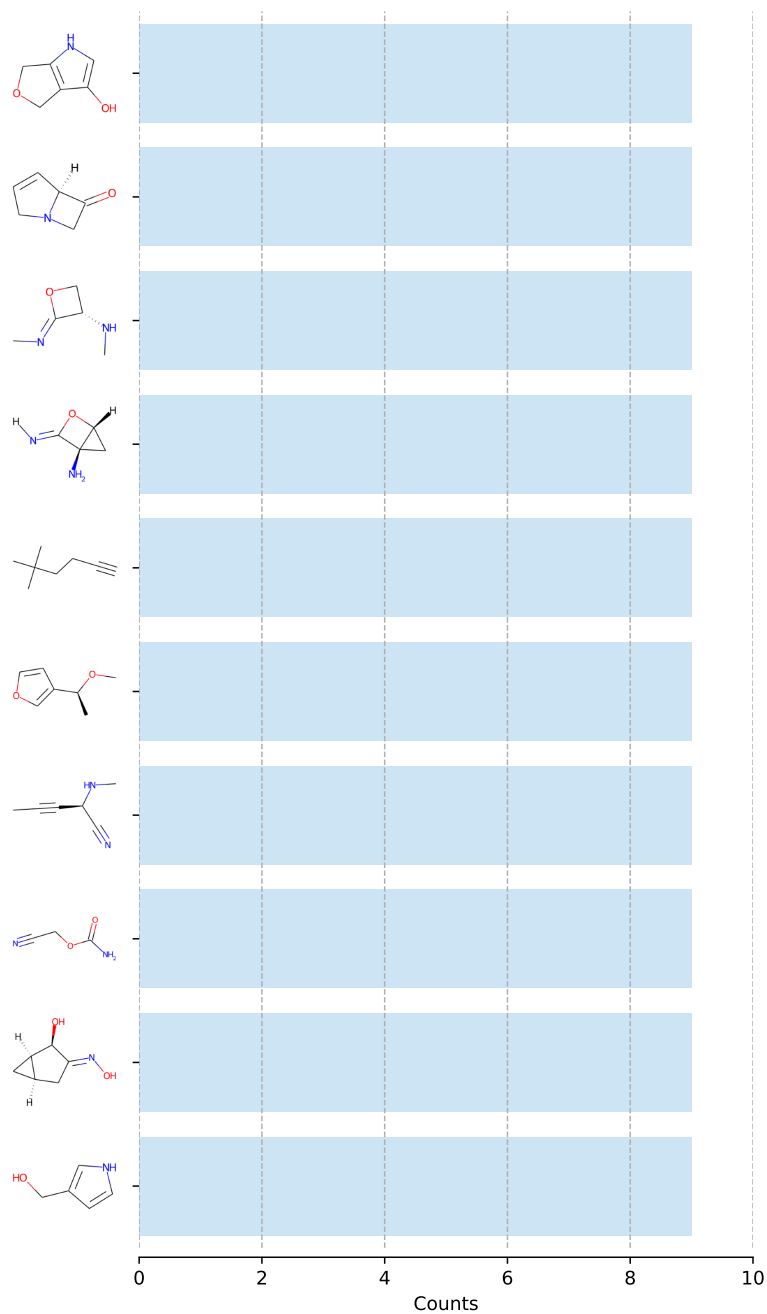


FIG. S6. Top 10 Common True Negative (TN) molecules ($\varepsilon_i < \varepsilon_{max}$ and $\sigma_i < \sigma_{max}$). The x-axis shows how often a molecule appear as TN for the different values of hyperparameter λ , the y-axis show the characteristic chemical structure.

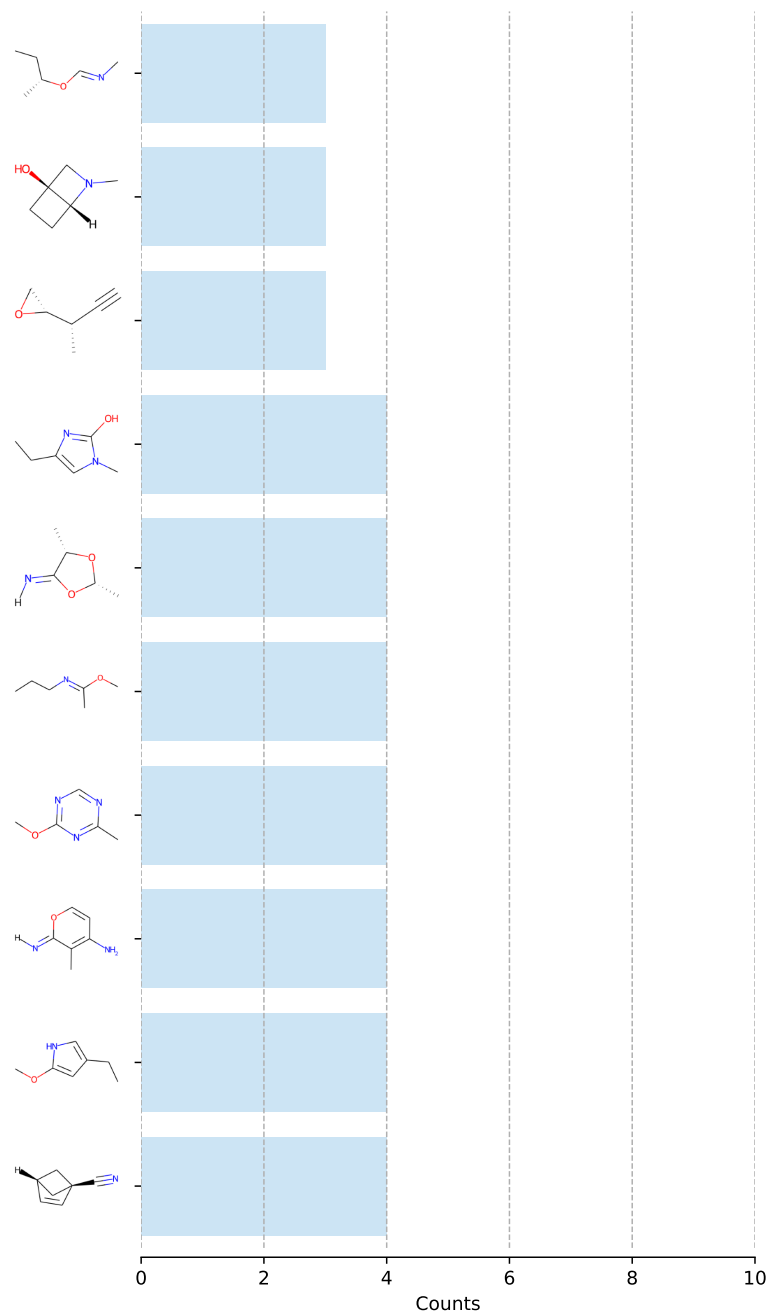


FIG. S7. Top 10 Common False Positive (FP) molecules ($\varepsilon_i < \varepsilon_{max}$ and $\sigma_i > \sigma_{max}$). The x-axis shows how often a molecule appear as FP for the different values of hyperparameter λ , the y-axis show the characteristic chemical structure.

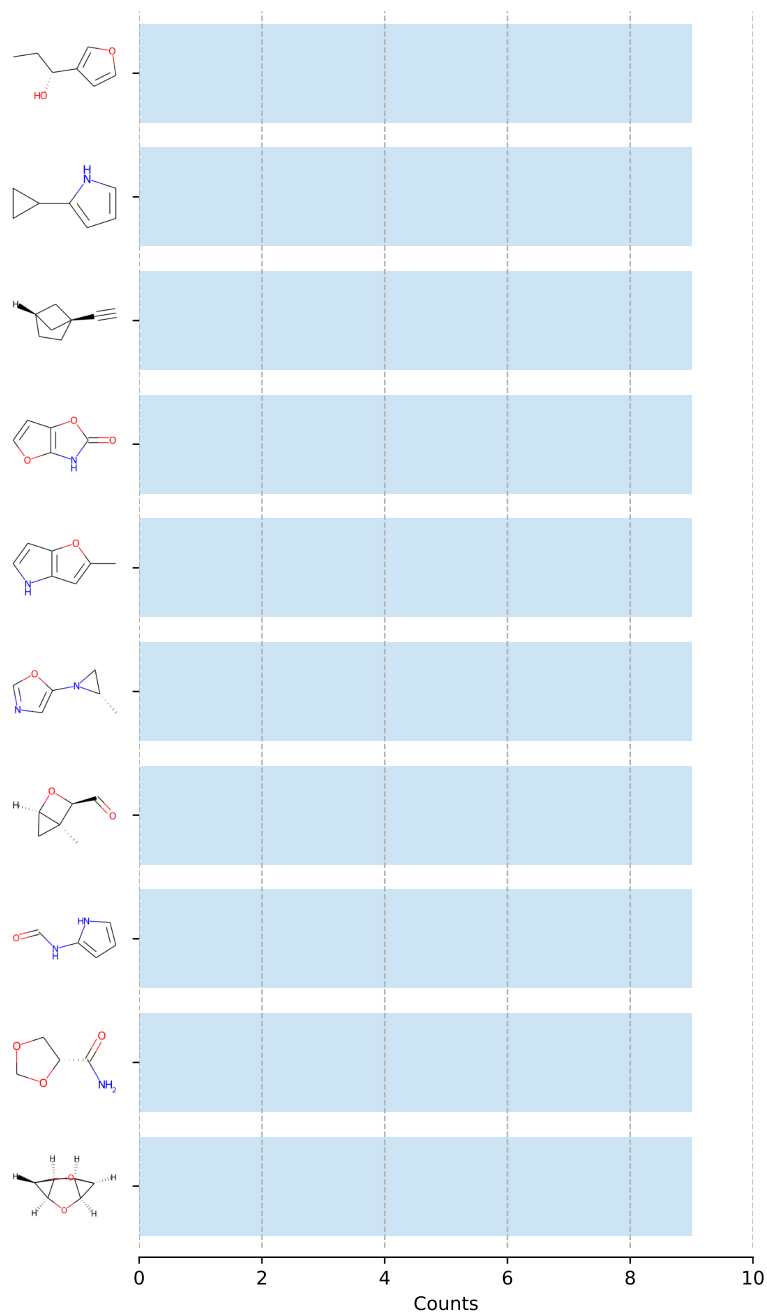


FIG. S8. Top 10 Common False Negative (FN) molecules ($\varepsilon_i > \varepsilon_{max}$ and $\sigma_i < \sigma_{max}$). The x-axis shows how often a molecule appear as FN for the different values of hyperparameter λ , the y-axis show the characteristic chemical structure.

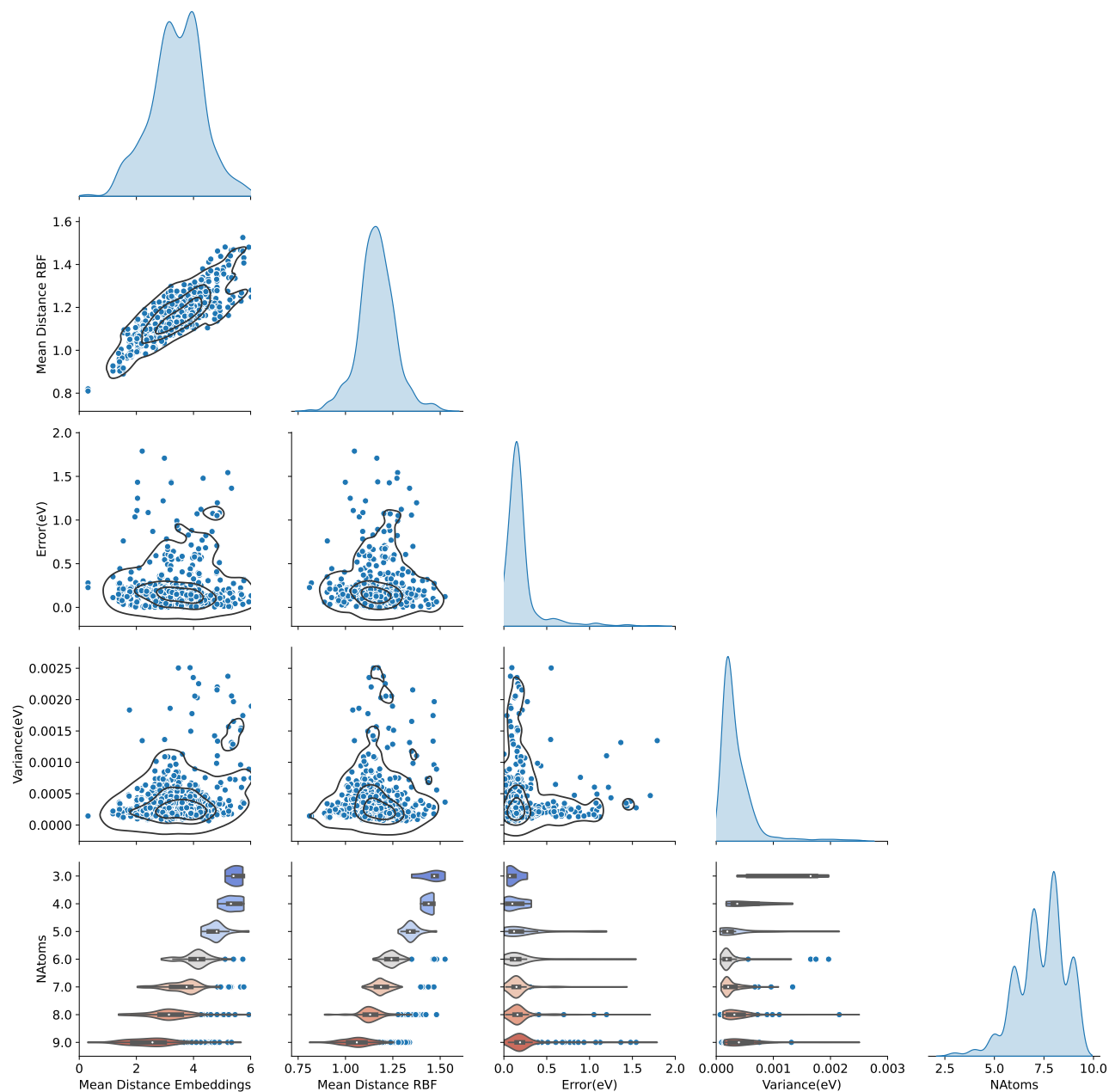


FIG. S9. Overview of the results for the evaluation of molecules on the tautobase for $\lambda = 0.2$. The diagonal of the figure shows the kernel density estimate of the considered properties (Mean Distance Embeddings, Mean Distance RBF, Error (eV), Variance (eV) and Number of Atoms). For each of the panels a correlation plot between the variable and a 2D kernel density estimate is shown. In the last row, violin plots for the different considered properties with respect to the number of atoms is shown.

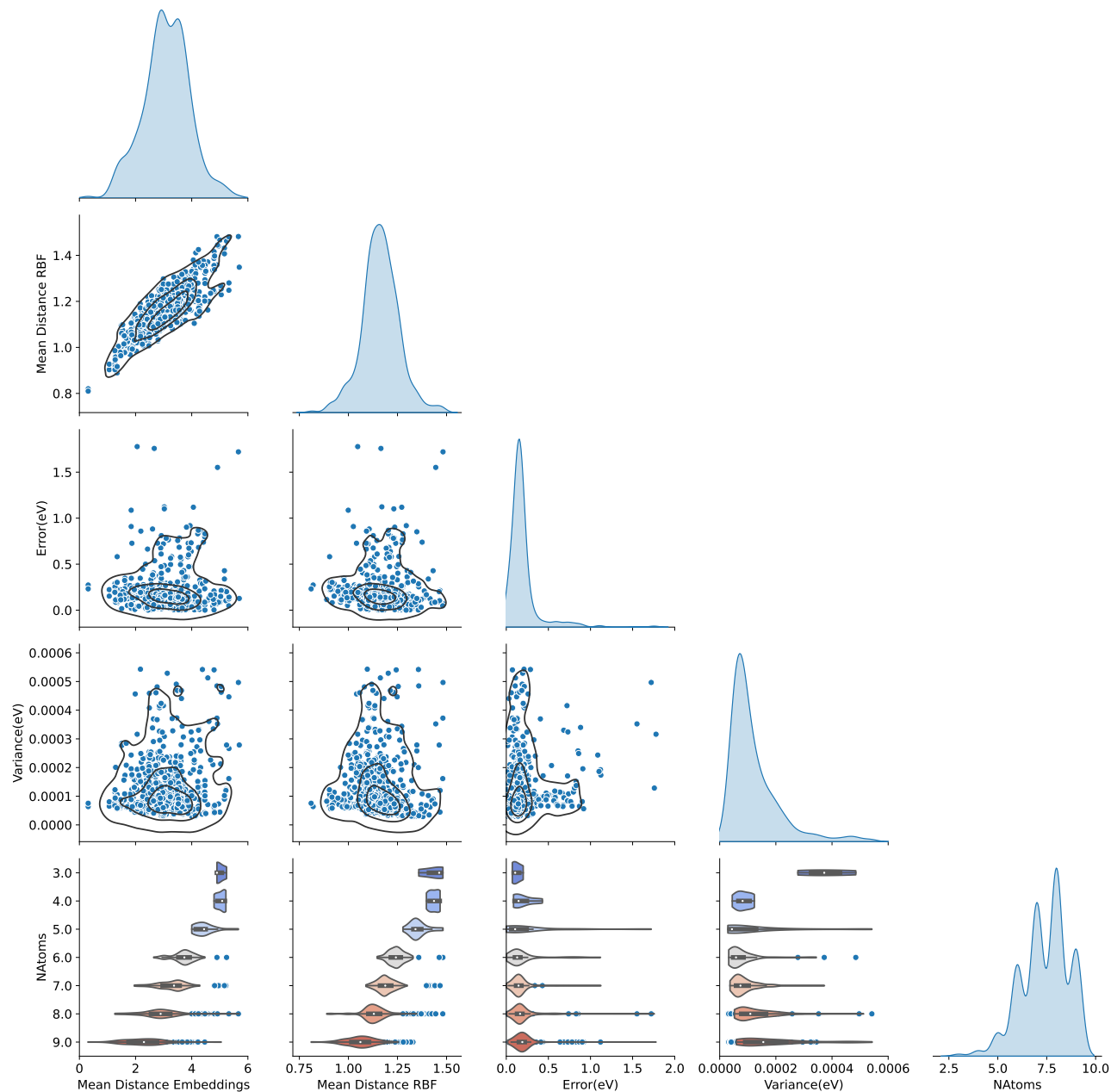
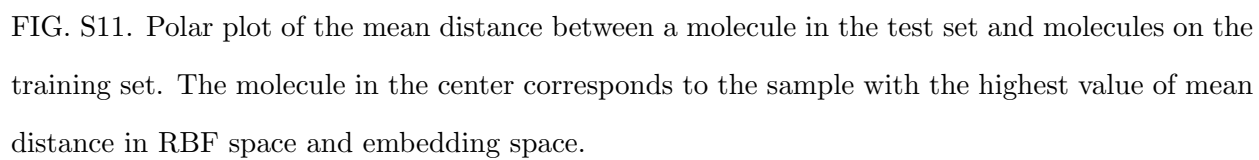


FIG. S10. Overview of the results for the evaluation of molecules on the tautobase for $\lambda = 0.4$. The diagonal of the figure shows the kernel density estimate of the considered properties (Mean Distance Embeddings, Mean Distance RBF, Error (eV), Variance (eV) and Number of Atoms). For each of the panels a correlation plot between the variable and a 2D kernel density estimate is shown. In the last row, violin plots for the different considered properties with respect to the number of atoms is shown.



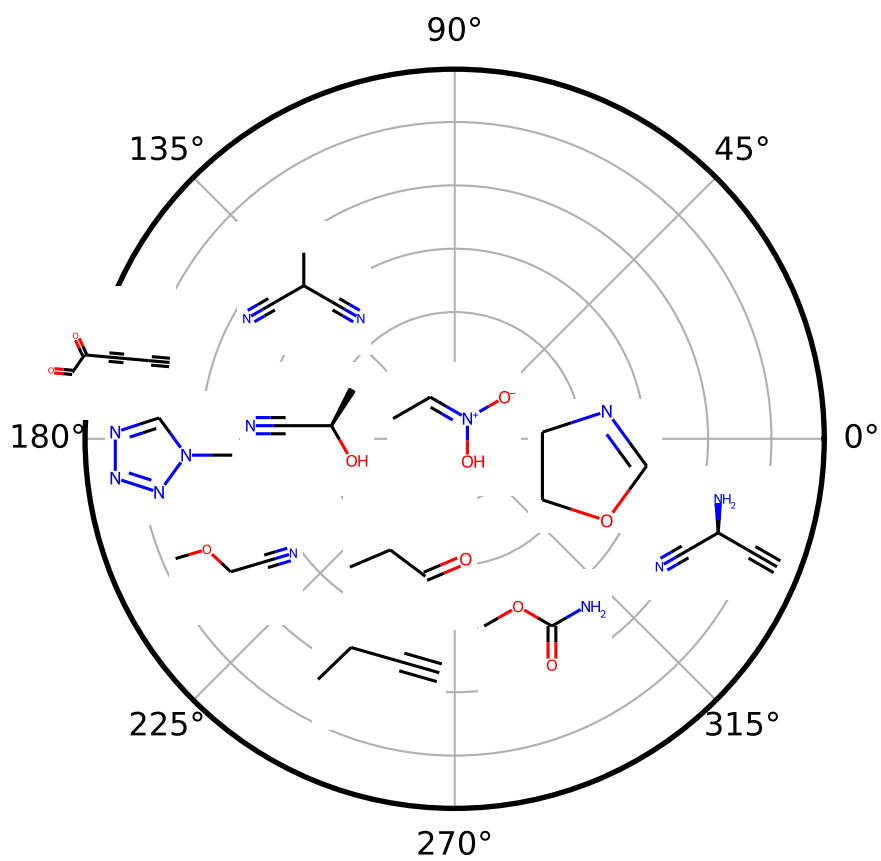


FIG. S12. Polar plot of the mean distance between a molecule in the test set and molecules on the training set. The molecule in the center corresponds to the molecule in the test set with the largest error on prediction.

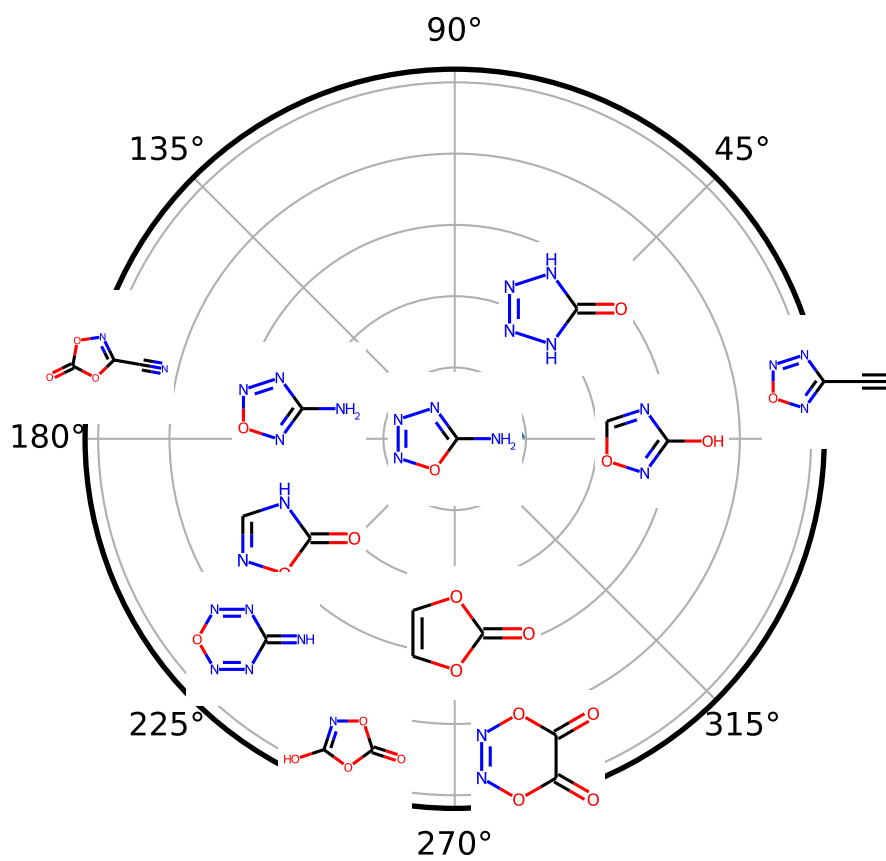


FIG. S13. Polar plot of the mean distance between a molecule in the test set and molecules on the training set. The molecule in the center corresponds to the molecule in the test set with the largest predicted variance

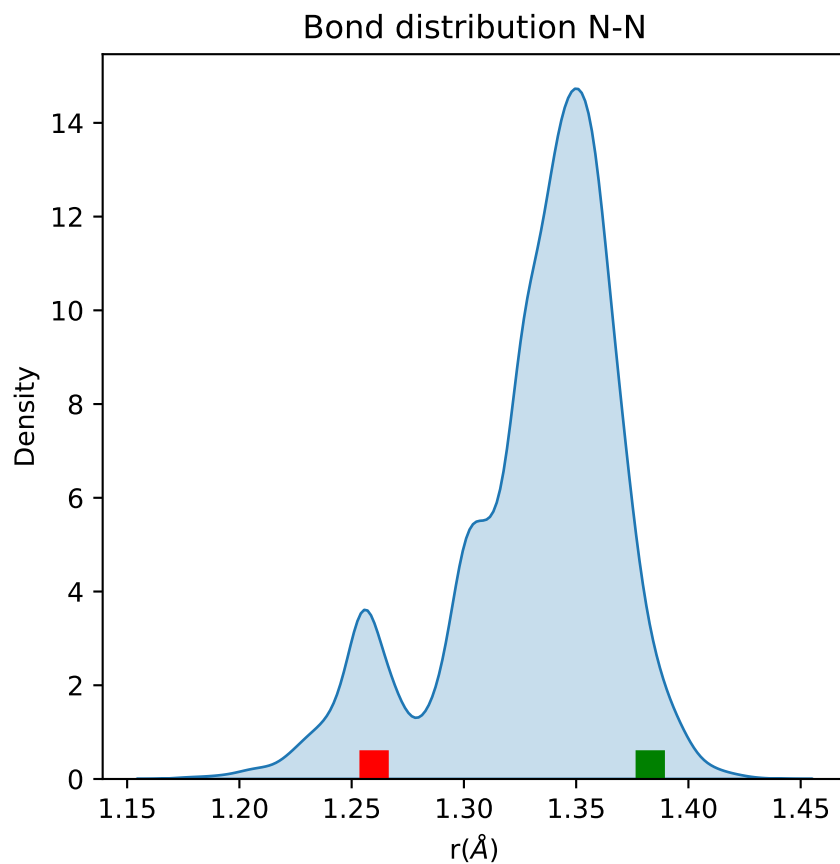


FIG. S14. N-N bond distribution from all molecules in the QM9 database⁶². The red point indicates the N-N bond distance for molecule A1 in Figure 8B and the green point indicates that for molecule B1.